TURBO

Scientific Journal

The first flight powered by Gas Turbine Engine.

On August 27th 1939, at Marienehe aerodrome, the Heinkel Airfield, near Rostock, Germany, a Heinkel He -178 airplane powered by a HeS 3B turbo jet made the first fly. A few days after became the WW 2.
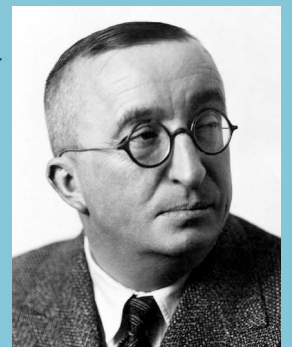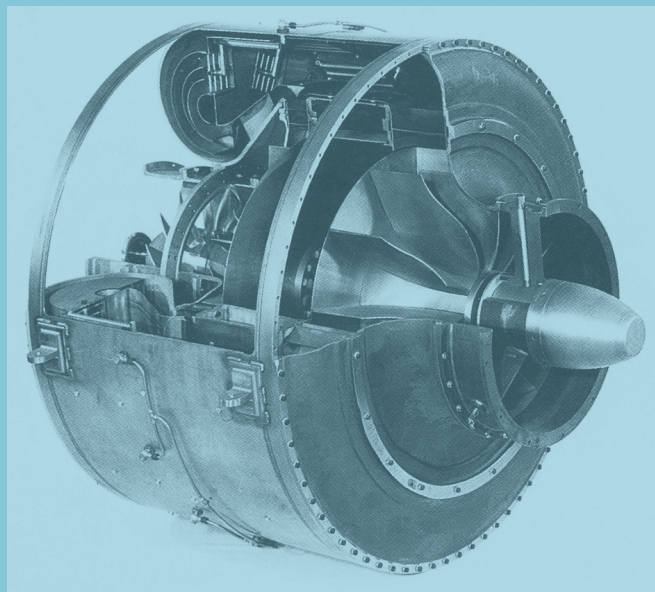
PASSION & COMPETENCE

Hans J. Pabst von Ohain
Inventor and Designer

Ernst Heinrich Heinkel
Entrepreneur

Erich Warsitz
Pilot

Max Hahn
Chef of manufacturer team

Editorial Board

CONTENT

Editorial
Singur cu ideea? (1)

Cunoașterea este izvor bogat pentru slava Creatorului și pentru bucuria omului.

Francis Bacon (1561-1627)

Cum cercetarea caută dintotdeauna inspirație în toate domeniile de cunoaștere, se naște astfel o sinergie care conduce la progres. Câmpul informațional al cunoașterii umane este doar unul, de aceea progresul umanității este asigurat de sinergia științei și culturii, capacitățile gândirii umane căutând și oferind nu doar mijloace de subzistență. Chiar prin obișnuința împărțirii culturii în materială și spirituală într-o unitate dialectică, universul cultural acționează întotdeauna ca un sistem de auto-dezvoltare și reprezintă o unitate de stil, de scop și de formă, ce cuprinde toate intențiile și rezultatele sale materiale și spirituale, ca expresie a spiritului unei epoci.

La sfârșitul anilor 1990, sociologul american Richard Florida a introdus conceptul de „clasă creativă" pentru a desemna apariția unei noi categorii de oameni în economia modernă a societății postindustriale. Identifica drept caracteristici ale reprezentanților clasei creative independență, mobilitate, libertate de mișcare, ca fiind necesare exprimării potențialului creativ.

Alfred Schütz (1899-1959), în lucrarea sa *Fenomenologia lumii sociale*, a încercat să definească legătura categoriilor științifice cu lumea vieții de zi cu zi. A studiat motivele acțiunii sociale, normele și metodele de cunoaștere cotidiană și structura comunicării umane. A considerat „fluxul de experiență", ca fiind principala modalitate de manifestare a conștientizării noastre - prin percepția senzorială. Percepția noastră asupra unui obiect, bazată pe cele cinci simțuri, nu ne poate spune decât că este. Numind un obiect, atribuindu-i semnificație, intrăm într-o anumită relație cu acesta, îl încadrăm în lumea creată de conștiința noastră. Astfel tranziția de la experiența senzorială la ordonarea și definirea logică, care are loc mai întâi în conștiință și apoi se manifestă în interacțiunea umană, este decisivă pentru sociologia fenomenologică.

Oamenii percep, definesc și explică mediul lor, construind o anumită lume socială. Imaginația proprie și activitatea directă, păstrează sau tinde să schimbe societatea, dând sens ori golind de sens inițiative, grupuri sau organizații. Spre deosebire de mediul natural, lumea socială încetează să mai existe dacă nu primește recunoașterea, asemenea unei idei : o idee neîmpărtășită = idee necunoscută/nerecunoscută.

Anul acesta în București se desfășoară Fusion AIR*, unicul proiect românesc de rezidențe artistice în institutele de cercetare, inițiat și organizat de Asociația Qolony, ce reunește patru instalații multimedia ce transpun concepte științifice în artă: patru artiști, în colaborare cu patru cercetători, în patru institute de cercetare, Institutul de Științe Spațiale, INCD pentru Textile și Pielărie, INCD pentru Fizica Materialelor și INCD pentru Fizica Laserilor Plasmei și Radiațiilor.

Rezultatul acestor rezidențe se află în expoziția *Fusion AIR – Structuri Convertibile*, la /SAC @ MALMAISON, un spațiu de inițiativă privată, spațiu - context de coproducții, cercetări și practici colaborative și transdisciplinare în științe, artele vizuale, artele performative și scenice, pentru a stabili un dialog direct și formator, prin demersul expozițional, al cercetării și promovării.

Instalațiile expuse

- **Arheologia invizibilului – despre particulele de energie înaltă care vin din Universul îndepărtat - Instalație multimedia**

Editorial
Singur cu ideea? (2)

Artistul Ciprian Ciuclea a realizat o instalație multimedia legată de reprezentarea materiei invizibile, a particulelor de energie înaltă, provenite de la supernovele care pătrund și interacționează cu atmosfera terestră. Cea care îl va ajuta să înțeleagă acest univers este dr. Gina Isar de la Institutul de Științe Spațiale, specialist în astrofizică, ce va oferi informații inedite și de interes pentru publicul larg despre aceste particule care călătoresc mii de ani lumină distanță până ajung la sol sub forma unor jerbe de particule elementare secundare, particule la care pământenii sunt expuși, fără să le simtă sau vadă.

- **Colagenul – molecula tinereții fără bătrânețe și patrimoniul scris al umanității - Instalație imersivă**

Aura Bălănescu artist interesat de cultura imaterială și dr. Elena Badea, INCD pentru Textile și Pielărie, cercetător chimist, specializat în studiul aspectelor materiale ale documentelor vechi, au realizat o instalație imersivă, ce folosește secretele tehnicii colagenului din pergamente, o țesătură capabilă să transfere informație. Expozeul Elenei Badea reprezintă ocazia care ne va face să reflectăm asupra complexității și perfecțiunii pergamentului, material destinat să supraviețuiască secolelor, pe care s-au suprapus istorii scrise și rescrise, fiecare dintre acestea de neșters, așteptând „lumina" propice care să le aducă din nou la iveală.

- **Mușchii artificiali. O abordare biomimetică pentru dezvoltarea de mușchi artificiali pentru soft-roboți**

Bioartista Floriama Cândea a realizat o serie de lucrări cu mușchi „artificiali", celule vii crescute pe suport organic sau anorganic, într-un demers la care i s-a alăturat dr. Ionuț Enculescu, din partea INCD pentru Fizica Materialelor, care argumentează că mușchii artificiali polimerici își propun să înlocuiască motoarele și pistoanele și să permită construirea unor așa numiți soft-robots care să ne facă viața mai ușoară.

- **Lumina purtătoare de informație - Instalație sonoră**

Peter Gate, muzician experimentalist, artist vizual și antropolog, alături de dr. Marian Zamfirescu INCD pentru Fizica Laserilor Plasmei și Radiațiilor, vor exemplifica efectul muzicii asupra celulelor vii, sub influența lumini purtătoare de informație. Instalația include și informații legate de felul în care laserul ajută la detectarea și investigarea substanțelor nocive, de la poluanții din aer și apă până la detectarea virusurilor, inclusiv SARS-COV-2.

https://qolony.eu/fusion-air/

*Vernisajul - vineri, 11 iunie, și sâmbătă, 12 iunie, cu începere de la ora 14.30, în cel mai nou spațiul expozițional din capitală, /SAC @ MALMAISON situat în strada Plevnei nr. 137C, et. 2, în prezența artiștilor ți a cercetătorilor. Accesul este liber, timp de trei săptămâni, până pe data de 3 iulie, inclusiv; program de vizitare: miercuri - vineri, orele 15:00 - 19:00.

Ec. Elena Banea

Editorial

Alone with the Idea? (1)

Knowledge is the rich storehouse for the glory of the Creator and the relief of man's estate

Francis Bacon (1561-1627)

As research has always sought inspiration in all areas of knowledge, a synergy is thus born that is leading to progress. The information field of human knowledge is singular, that is why human progress is ensured by the synergy of science and culture, while the capacities of human thinking are seeking and offering not only means of subsistence.

Even through the habit of dividing culture into material and spiritual within a dialectical unity, the cultural universe always acts as a system of self-development and represents a unity of style, purpose and form, encompassing all its material and spiritual intentions and results, as an expression of the spirit of an age.

Alfred Schütz (1899-1959), in his work Phenomenology of the Social World, tried to define the connection of scientific categories with the world of daily life. He studied the reasons for social action, the norms and methods of daily knowledge and the structure of human communication. He considered the "flow of experience" as the main way to manifest our awareness - through sensory perception. Our perception of an object, based on the five senses, can only tell us that it exists. By naming an object and assigning meaning to it, we actually interact with it, we frame it into the world created by our own consciousness. Thus, the transition from sensory experience to logical ordering and definition, which takes place first in consciousness and then manifests itself through human interaction, is decisive for phenomenological sociology. People perceive, define and explain their environment, by building a certain social world. Individual imagination and direct activity, either preserve or tend to change society, giving meaning or emptying of any meaning initiatives, groups or organizations. Unlike the natural environment, the social world ceases to exist unless it receives recognition, as it happens with an idea: an unshared idea = unknown / unrecognized idea.

This year in Bucharest is going to take place Fusion AIR *, the only Romanian project of artistic residencies developed in research institutes, which is initiated and organized by the Qolony Association and which brings together four multimedia installations that transpose scientific concepts into art: four artists, in collaboration with four researchers, in four research institutes, the Institute of Space Sciences, INCD for Textiles and Leather, INCD for Materials Physics and INCD for Plasma and Radiation Laser Physics.

The result of these residencies is to be found in the exhibition Fusion AIR - Convertible Structures, at / SAC @ MALMAISON, a private initiative environment, space - context co-productions, research and collaborative and transdisciplinary practices in science, visual arts, performing and acting arts, to establish a direct and formative dialogue between research and promotion by means of this exhibition approach.

Exposed installations

- **The Archeology of the Invisible - About High Energy Particles Coming from the Distant Universe - Multimedia Installation**

The artist Ciprian Ciuclea created a multimedia installation related to the representation of invisible matter, of high energy particles coming from supernovae that penetrate and interact with the Earth's atmosphere.

Editorial
Alone with the Idea? (2)

The one who will help him understand this universe is Dr. Gina Isar from the Institute of Space Sciences, a specialist in astrophysics, who will provide unique and interesting information for the general public concerning these particles that travel thousands of light years until they reach the ground in the form of sheaves of secondary elementary particles, particles to which earthlings are exposed to without feeling or seeing them.

- **Collagen - the Molecule of Eternal Youth and the Written Heritage of Humanity - Immersive Installation**

Aura Bălănescu, an artist interested in immaterial culture and Dr. Elena Badea, INCD for Textiles and Leather, chemist researcher, specialized in studying the material aspects of old documents, created an immersive installation that uses the secrets of collagen technique in parchments, a fabric capable of transferring information. Elena Badea's presentation is an opportunity that will make us reflect on the complexity and perfection of parchment, a kind of material meant to overcome the centuries, on which overlapped written and rewritten histories, each of them indelible and waiting for the right "light" to bring them back to life.

- **Artificial Muscles. A Biomimetic Approach to the Development of Artificial Muscles for Soft-Robots**

Bioartist Floriama Cândea developed a series of works by using "artificial" muscles, living cells grown on organic or inorganic support, in an approach joined by Dr. Ionuț Enculescu, from INCD for Materials Physics, who supports the idea that polymeric artificial muscles are aiming to replace engines and pistons and to allow the construction of so-called soft-robots that are meant to make our lives easier.

- **Knowledge Carrying Light - Sound Installation**

Peter Gate, an experimental musician, visual artist and anthropologist, together with Dr. Marian Zamfirescu from INCD for the Physics of Plasma and Radiation Lasers, will exemplify the effect of music on living cells, under the influence of knowledge-carrying light. The facility also includes information concerning laser detection and investigation of harmful substances, from air and water pollutants to virus detection, SARS-COV-2 included.

https://qolony.eu/fusion-air/

*The opening day - Friday, June 11, and Saturday, June 12, starting at 2.30 pm, in the newest exhibition space in the capital, / SAC @ MALMAISON, located in Plevnei Street, no. 137C, et. 2, in the presence of artists and researchers. Access is free for three weeks, until July 3, included; visiting hours: Wednesday - Friday, 15:00 - 19:00.

Ec. Elena Banea

HYBRID VERTICAL AXIS WIND TURBINE NUMERICAL INVESTIGATION

Mihnea GALL[1], Ioana BUCUR[1]

ABSTRACT: Hybrid vertical axis wind turbines (VAWT) are a promising concept among wind machines as they combine different features from several types of VAWTs. Despite being cost effective and reliable, the H-type Darrieus VAWT alone are still operating under the concern of their self-starting capability. The aim of this paper is to assess the performance of a hybrid H-type Darrieus-Savonius VAWT using CFD methods in order to study its enhanced features for small-scale and domestic applications compared to a classical H-type VAWT. The unsteady 2D simulation is computed using Ansys Fluent by employing the SST k-ω turbulence model. Whereas the computational domain for both the stator and the H-type Darrieus rotor was made in ICEM CFD, Ansys Meshing was used for the Savonius rotor. The hybrid wind turbine is studied numerically at seven different values of TSR, thus plotting the torque coefficient for a whole rotation of the VAWT. Moreover, after post-processing the results, the power coefficient was obtained for each TSR. The vortical pattern was computed and analysed for two values of TSR at different angles of rotation

1. INTRODUCTION

In the last few decades, the increasing awareness concerning the greenhouse gases and their effect – global warming - has led to the idea of reducing the worldwide dependency on fossil fuels [1]. Consequently, not only European policies in such direction were developed, but also worldwide measures were taken [2]. As a result, researchers are encouraged to turn their attention to renewable energy sources.

Wind energy is of high potential in a lot of regions worldwide and it has to be efficiently exploited by wind machines. There are both vertical axis and horizontal axis wind turbine configurations which particularly bring their own features and advantages. However, when it comes to small turbines, reduced noise level in operation and omni-directionality, vertical axis wind turbines (VAWTs) are much more preferred [3].

Standard VAWT configurations (Darrieus, Savonius, H-type Darrieus or Giromill) can be combined into a hybrid solution which brings along the features of two VAWTs, thus obtaining a better efficiency in operation. This idea is not quite new as in 1978, Paraschivoiu et al. [4] conducted a theoretical study on the possibility to design a hybrid VAWT made of two coaxial turbines – one of Savonius type, whereas the other of screw type. They succeeded to show that the efficiency of a hybrid wind turbine may be higher than that obtained from just a simple device.

In the recent years, several studies on hybrid VAWTs have proposed a combination between H-type and Savonius which may be useful for low wind speed applications by providing higher efficiency than the single Savonius rotor [5]. Whereas Savonius, a drag-type wind machine, is well known for its self-starting

---

[1]Romanian Research and Development Institute for Gas Turbines COMOTI, Bucharest, Romania

capability with low torque requirement, the H-type rotor, a lift-driven wind device, presents higher power coefficient than Savonius.

Bhuyan and Biswas [6] designed a hybrid VAWT which exhibits both self-starting and high power coefficient by employing a three unsymmetrical bladed H-rotor along with a Savonius rotor. They underwent an experimental study in the wind tunnel in order to determine the optimum solution regarding the overlap configuration of the Savonius rotor as part of the hybrid wind device. However, they concluded that the integration of Savonius rotor resulted in self-starting capacity of the whole system, but a reduction in power generation capacity was recorded, too. A comparative power coefficient versus tip speed ratio plot between the simple H-rotor and the hybrid H-Savonius with null overlap at Reynolds $1.92*10^5$(10 m/s) revealed a 0.18 power coefficient for the hybrid configuration at TSR 2, while the classical H-type configuration stayed 0.1 higher at 0.28 power coefficient at the same TSR. This penalty in efficiency for the hybrid setup appeared to be the same for the TSR range 2-3 that was investigated. However, the authors concluded that the hybrid configuration could surpass the efficiency of the classical one if further optimized, finding that 0.15 is the optimum overlap condition for the Savonius rotor part.

In their experimental study in the wind tunnel, Gupta et al. [7] compared the performance of a single three bucket Savonius configuration with a hybrid three bucket Savonius - three bladed Darriues VAWT. They reported a maximum power coefficient of 51% for the combined rotor with no overlap which was higher than the efficiency of the single Savonius at various overlap positions.

Jacob and Chatterjee [8] bring their contribution to hybrid VAWT design not only by deriving an expression for an optimal radius ratio of the rotors, but also by proposing a methodology for designing such kind of wind machines.

In his PhD thesis, Ahmedov [9] managed to compare the CFD results for a hybrid VAWT with the experimental results. He concluded that CFD is a suitable tool to predict the operation and the performance of a VAWT. Moreover, he stated that the 2D approach gives a detailed view of the formation, development and interaction of the vortex detaching from the blades.

Also interested in hybrid VAWTs, Wakui et al. [10] revealed in their paper that the hybrid turbine with the Savonius rotor placed inside the Darrieus rotor is recommended for stand-alone small-scale systems. This type of configuration exhibits fine operating behaviour when changes in wind speed take place and moreover it allows a compact design due to the reduced rotational axis.

As both numerical and experimental studies on hybrid VAWTs were made until now, the aim of this paper is to continue the already existing works with a methodology to assess the performance of hybrid wind plant using CFD methods. The studied hybrid VAWT combines a three bucket Savonius type (inner zone) with a three bladed H-type Darrieus type (outer zone).

2. NUMERICAL SIMULATION

2.1. Machine configuration

This paper evaluates numerically the performance of a hybrid VAWT which consists of a combination between a Savonius rotor (inner zone) and a H-type Darrieus one (outer zone) mounted on a common shaft (Fig. 1).

The design of the outer H-type Darrieus rotor followed the fundamental design theory of wind turbines using the conservation of mass and energy in a wind stream. Starting from a 3 kW power, an upstream wind velocity of 10 m/s, a 0.32 nominal power coefficient, a 0.5 solidity and a 1.5 height to diameter ratio, the geometrical features for the H-type rotor were defined. The ratio between the two rotors diameters was set to 3.4 which is close to the one chosen in [6]. The geometrical parameters of the two rotors can be found in Table 1 and Table 2, respectively. A detailed draft on the two rotors can be found in Fig. 2.

Table 1 H-type Darrieus rotor parameters

H-type Darrieus rotor	
Diameter	3.2 m
Rotor height	4.8 m
Number of blades	3
Chord	0.3 m
Airfoil	NACA 0018

Table 2 Savonius rotor parameters

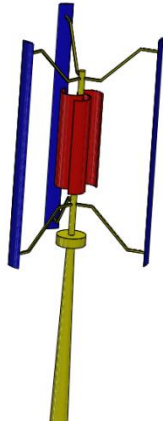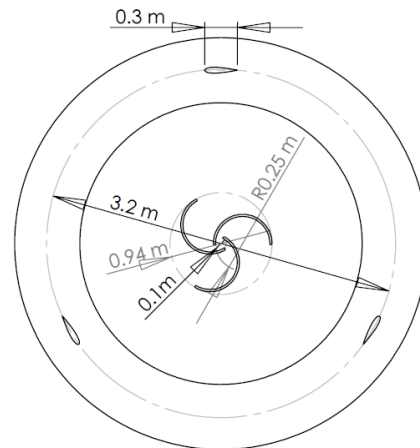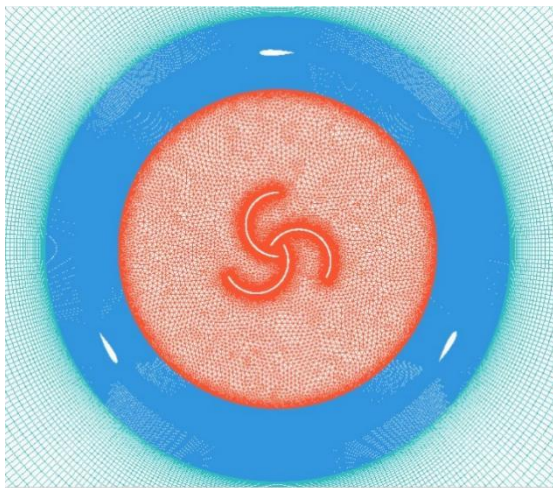| Savonius rotor	
Diameter	0.94 m
Shaft diameter	0.1 m
Number of blades	3
Blade radius	0.25 m
Blade thickness	0.02 m

Fig.1 Hybrid VAWT 3D model

**Fig.2 Detailed domain configuration - rotors**

2.2. Domain details

The computational domain for the hybrid VAWT is divided into three parts: the stator, the H-type Darrieus rotor and the Savonius rotor (Fig. 2). Whereas the Savonius domain is circular (0.94 m diameter), the H-type Darrieus domain is annular (3.2 m diameter). The annular stator diameter was chosen as 10 times the H-type Darrieus rotor diameter to allow vortical structures dissipate before reaching the outmost boundary. Moreover, this stator diameter guarantees there is no influence of the imposed boundary conditions on the fluid evolution on the rotor domain and so the turbine efficiency figures are not numerically altered.
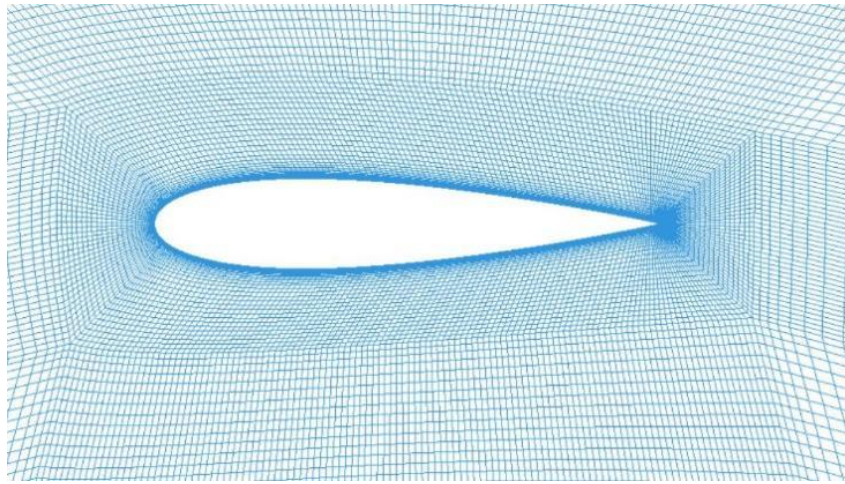
2.3. Mesh

The quadrilateral structured computational grid for both the stator and the H-type Darrieus rotor was generated using ICEM CFD by employing blocking function (Fig. 3a). As the accuracy of the numerical solution depends a lot on the near wall region mesh, the size of the first cell near the blade was set to $5*10^{-5}$ m so as to achieve an y^+ of 1 (Fig. 3c). In contrast, a triangular unstructured computational grid for the Savonius rotor was made using Ansys Meshing in order to obtain an accurate discretization of the curved blades (Fig. 3b). The high curvature of the Savonius blades would lead to poor quality mesh elements in case a structured grid would have been used, thus introducing numerical errors. Using a partially unstructured mesh is not an uncommon practice when researching wind systems, this approach was successfully used in recent years as highlighted in [11]. An inflation to the blade was set up too and the first cell size is $5*10^{-5}$ m. After putting all the mesh parts together, the whole computational domain has about 250000 elements. The interface between the structured mesh (stator and H-type rotor) and the unstructured mesh is solved by a merging procedure.

a)
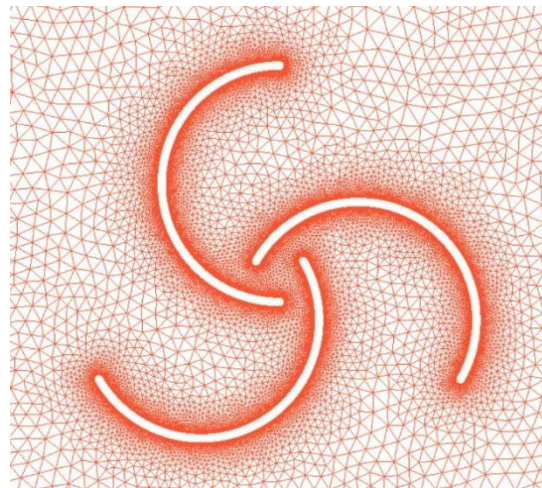
b)

c)
Fig. 3 Mesh details a) Rotors b) Savonius blade c) Darrieus blade

2.4. Boundary conditions and simulation setup

The unsteady flow through the hybrid VAWT is studied by solving the averaged incompressible Navier-Stokes equations using SIMPLEC algorithm. For Reynolds stress tensor modelling purposes, the SST k-ω turbulence model was used along with low Re correction and curvature correction. The estimated Reynolds number range using the H-type rotor blade chord as a reference and air at standard conditions belongs to $3*10^5$ for TSR 1.5 up to $9*10^5$ for TSR 4.5. The SST k-ω turbulence model successfully blends the Wilcox k-ω turbulence model which is able to capture the boundary layer flow with the k-ε model which shows stability in the far field region.
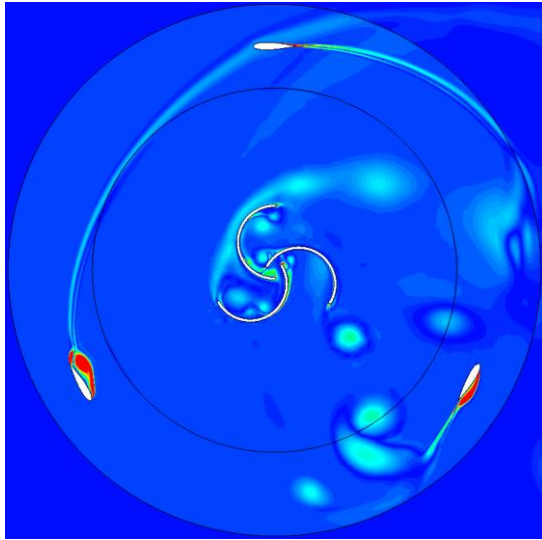
As described in the previous section, the two rotors and the stator were defined as fluid. Regarding the materials, the fluid properties are the same of the air, while the properties of the solid elements are the ones of aluminum (default setting). For both the H-type Darrieus blade and the Savonius blade, the wall boundary condition was chosen along with no slip shear condition. The two interfaces between the three subdomains were defined using the Ansys Fluent feature "Mesh Interface".

For the velocity inlet boundary condition, the value of the constant velocity magnitude was set to 10 [m/s], having only the X-component of the flow direction. The rotor subdomain was defined using "Mesh Motion" in Ansys Fluent and it had a constant rotational velocity [rad/s] set, correspondent to the value of TSR.
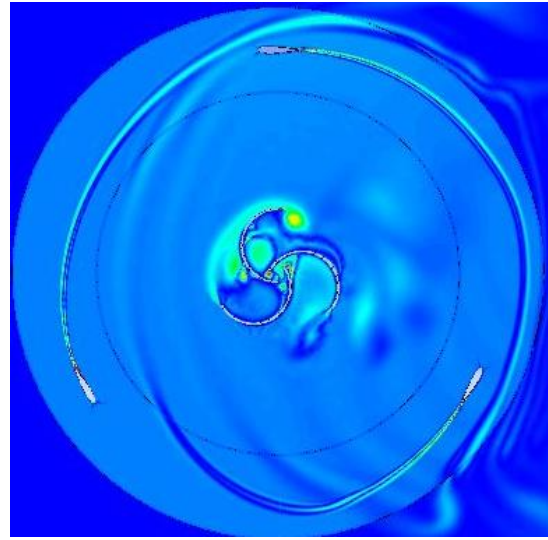
3. RESULTS AND DISCUSSIONS

In Fig. 4, the vorticity magnitude is shown for 2 different TSR values (2 and 4 respectively) recorded at 4 different positions of the hybrid VAWT turbine (0^0, 30^0, 60^0, 90^0). The TSR 2 and 4 results were considered relevant as TSR 2 represents the point before the hybrid turbine registered higher power coefficients (for TSR 2.5, 3 and 3.5 the power coefficient had close values above 0.5) and TSR 4 represents the point from which the power coefficient starts to decline. It is relevant to present the vortical contours for these tip speed ratios, in order to assess blade-to-blade interaction, that is considered one factor for decreasing power coefficient. An overall strong vortical pattern can be observed in the vicinity of the Savonius rotor placed in the inner zone of the hybrid turbine. In contrast, the H-type Darrieus rotor blades show a long wake that follows the circumference along with strong separation bubbles for several positions (30^0, 60^0, 90^0).

In comparison with the contours plotted for TSR 4, the TSR 2 contours present a more intense vortical activity. This fact leads to a visible difference in performance of the hybrid VAWT as shown in Fig. 6: whereas the power coefficient for TSR 4 is about 0.5, the power coefficient for TSR 2 is just about 0.3. Therefore, the hybrid studied turbine behaves better for higher values for the TSR, contrasting with the Savonius operating range, as it performs better for lower tip speed ratios. As a result, the hybrid turbine is closer to the operational range of H-Darrieus VAWTs than to that of Savonius.

a)

a')
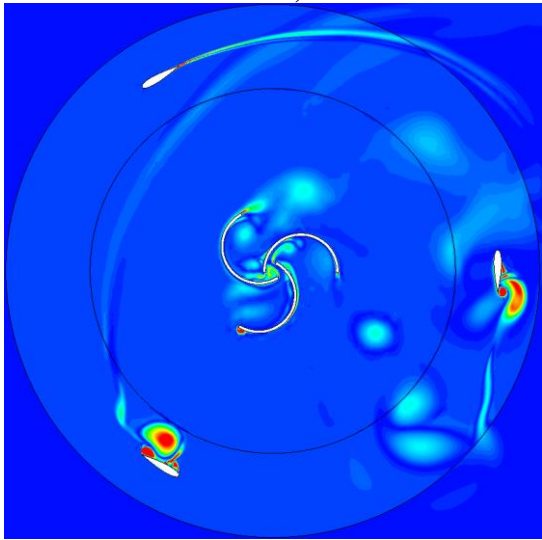
b)
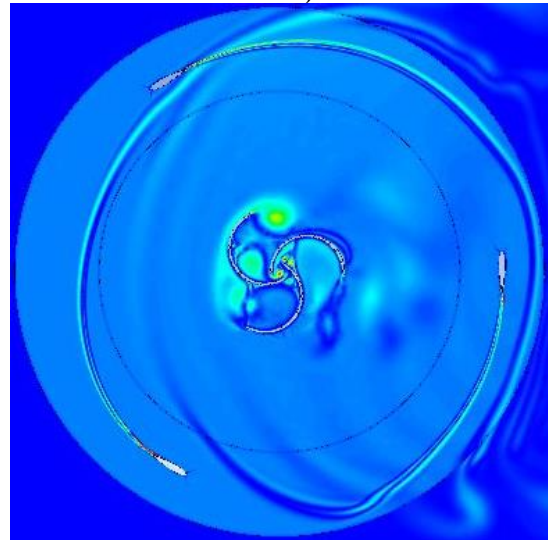
b')
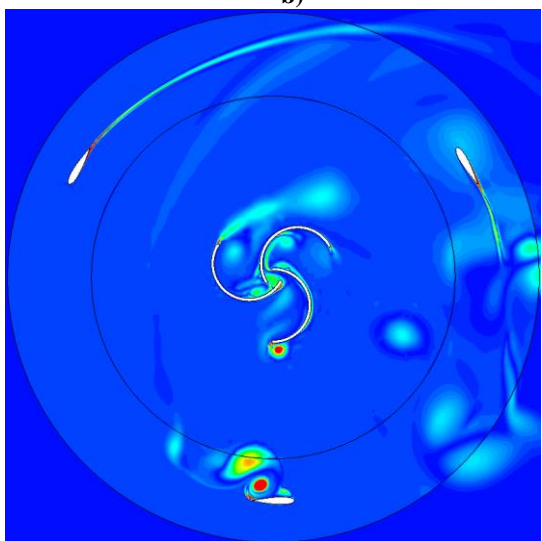
c)
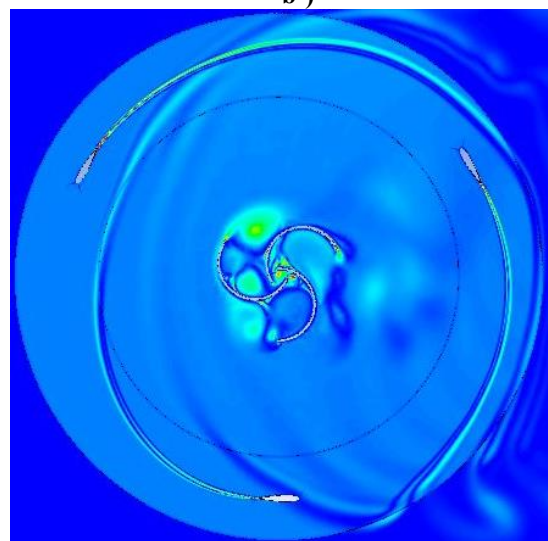
c')
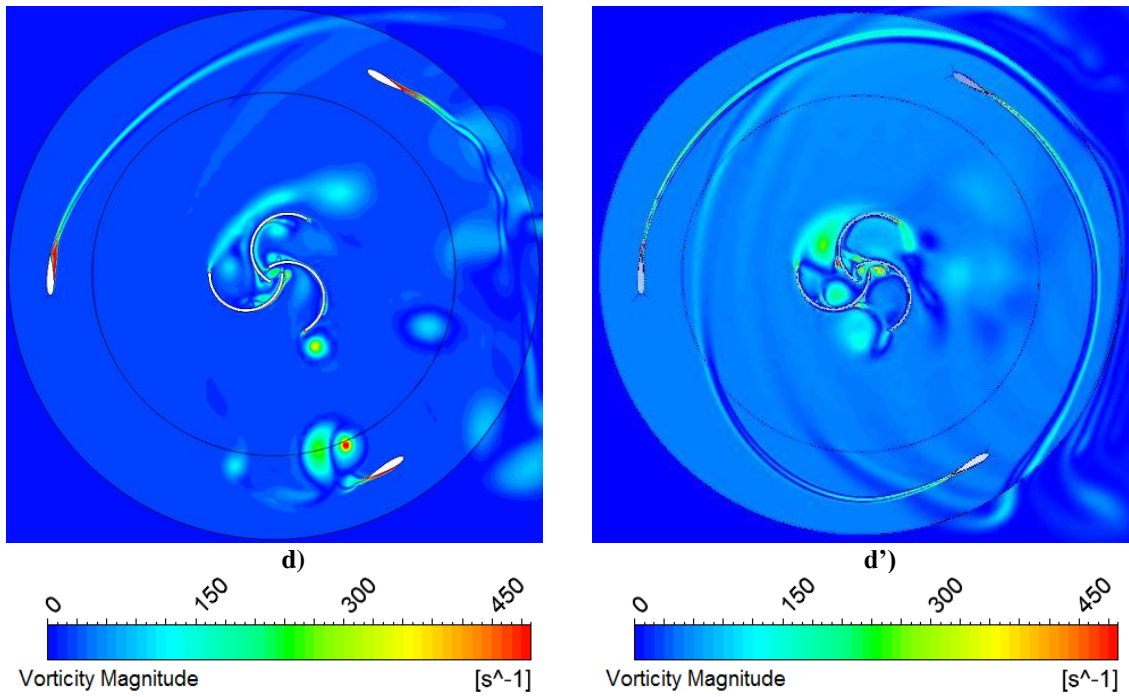
Fig 4. Vorticity Magnitude: a) TSR=2 and θ=0°; a') TSR=4 and θ=0°; b) TSR=2 and θ=30°;
b') TSR=4 and θ=30°; c) TSR=2 and θ=60°; c') TSR=4 and θ=60°;
d)TSR=2 and θ=90°; d')TSR=4 and θ=90°;

Fig.5 presents the torque coefficient variation of the H-type Darrieus rotor within a whole rotation of the hybrid VAWT for seven different tip speed ratio (TSR) values. For periodicity purpose, the values plotted in Fig.5 correspond to the fifth full revolution of the assessed turbine [12].

The periodicity of this graph can be easily noticed for each TSR value. Furthermore, there are three torque coefficient peaks which correspond to the three bladed configuration of the H-type Darrieus rotor. It can be observed that the higher the TSR the lower the amplitude of the torque coefficient which has great effect on the power coefficient variation plotted in Fig. 6.

Fig. 5 Torque coefficient for different values of TSR

The power coefficient variation with the tip speed ratio (TSR) was plotted in Fig. 6. The power coefficient refers to the hybrid configuration as a whole and it was obtained by multiplying the TSR with its corresponding average torque coefficient from Fig. 5. From a first glance, the maximum power coefficient of about 0.54 is recorded at 3.5 TSR. At a closer look, one can notice that there is a sharp increase in the power coefficient up to 2.5 TSR; moreover, a slight fluctuation around 0.52 can be seen between 2.5 and 3.5 TSR and finally a minor decrease to 0.45 is recorded at 4.5 TSR. The plateau observed between TSR 2.5 and 3.5 appears as a result of the Savonius inclusion which acts as a brake thus deteriorating the power generating capacity of the hybrid configuration.
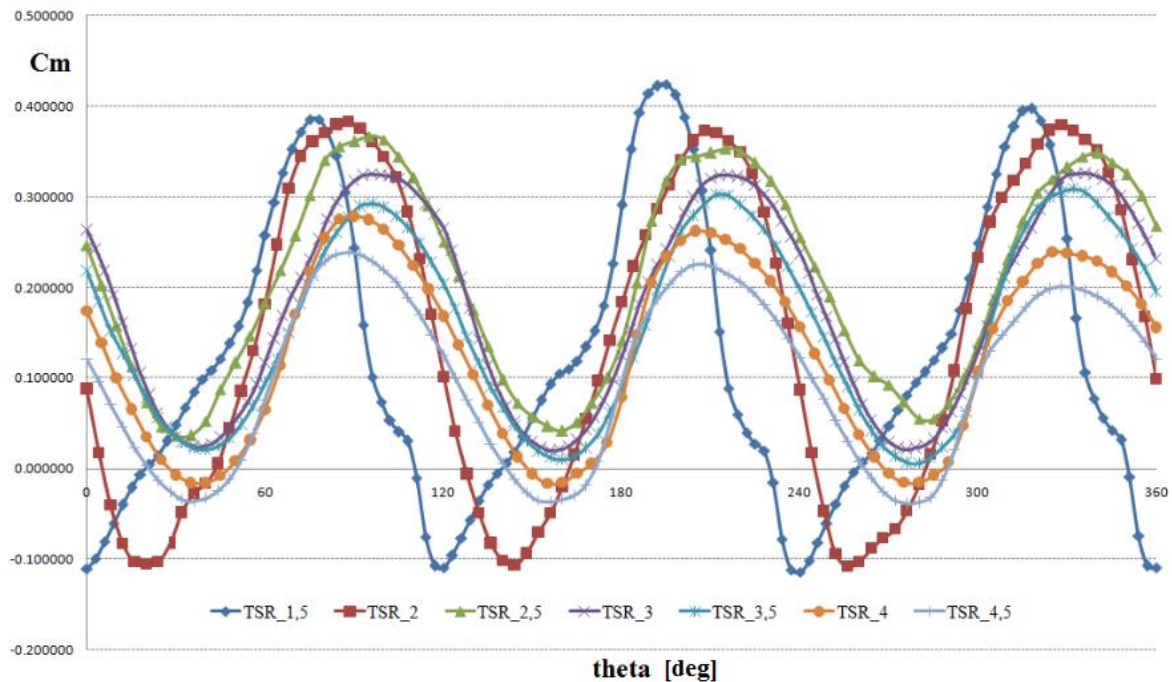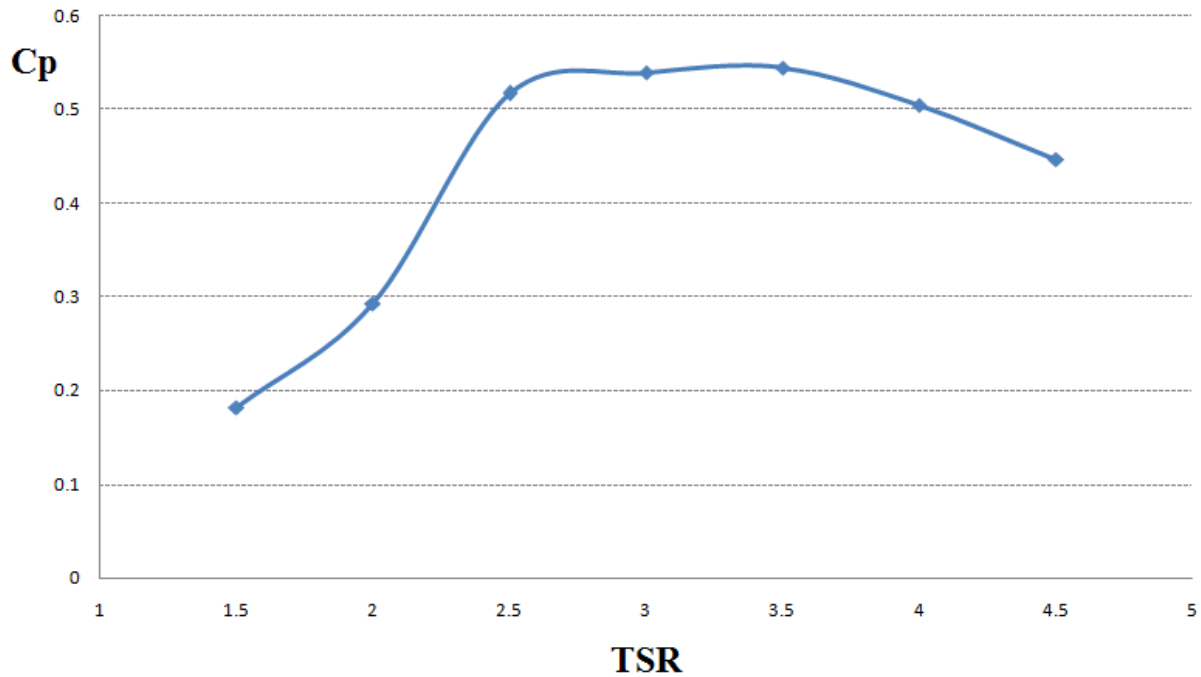

Fig. 6 Power coefficient variation

4. CONCLUSIONS

The main purpose of this study was to numerically evaluate the performance of a hybrid H-type Darrieus-Savonius vertical axis wind turbine. One main premise adopted from current state of the art was that such a configuration improves the self-starting capabilities of a classic H-Darrieus geometry by means of a Savonius rotor inclusion on the same axis of rotation, thus obtaining the aforementioned hybrid H-type Darrieus-Savonius turbine. The design parameters of the H-type rotor refer to a range of small-scale domestic applications, such as public lighting or small enterprises.

As previously stated, the goal of the conducted study was to numerically investigate the performance of the developed hybrid VAWT. The analyzed geometry yielded promising numerical results, with a peak in power coefficient of 0.54 at TSR 3.5. Moreover, such hybrid VAWT possesses self-starting feature along with high power coefficient simultaneously.

The elaborated paper contributes to the general know-how regarding the setting up of a methodology for CFD simulations on hybrid VAWTs, presenting in detail the approach for mesh generation and the case setup for the simulations. This is going to be valuable for future optimisation studies on similar wind systems in order to determine the optimum geometrical parameters for the two rotors.

To conclude, the current paper succsessully demonstrates that the penalty in efficiency generated by introducing a Savonius rotor into a H-Darrieus one is acceptable, as the numerical results showed high values for the power coefficient for the studied hybrid configuration. Thus, this paper provides a starting point for a more in-depth investigation towards small scale VAWT for domestic applications with enhanced features in starting conditions.

5. FURTHER WORK PERSPECTIVES

As the numerical computations are in general sensitive to mesh quality and size, a grid dependency study will be performed in future papers in order to assess its possible influence on the current case under investigation.

Additionally, a detailed analysis on the effect of the overlap parameter of the Savonius rotor may be also performed. The overlap represents an optimisation parameter for the hybrid configuration. In general, a Savonius inclusion into a classical H-type Darrieus configuration improves the self-starting capability, but it affects the power generating capacity. A detailed overlap optimisation could solve this issure. Future work also includes the per-se investigation of the self-starting capabilities of the developed model, in order to assess its improvement, unsing special methods such as 6DOF.

REFERENCES

[1]   M.S. Dresselhaus, I.L. Thomas, *Alternative energy technologies*, Nature, 2001, Nature Publishing Group

[2]   W.D. Nordhaus, *To Slow or Not to Slow: The Economics of The Greenhouse Effect*, The Economic Journal, Vol. 101, No. 407 (Jul., 1991), pp. 920-937

[3]   *https://en.wikipedia.org/wiki/Vertical_axis_wind_turbine#Advantages*

[4]   I. Paraschivoiu, E. Bilgen, F. da Matha Santanna, *Theoretical study of a hybrid wind turbine*, 1978

[5]   A. Pallotta, D. Pietrogiacomi, G.P. Romano, *HYBRI - A combined Savonius-Darrieus wind turbine: Performances and flow fields*, 2020, Energy, Vol. 191

[6]   S. Bhuyan, A. Biswas, *Investigations on self-starting and performance characteristics of simple H and hybrid H-Savonius vertical axis wind rotors*, 2014, Energy Conversion and Management 87 (2014) 859–867

[7]   R. Gupta, A. Biswas, K.K. Sharma, *Comparative study of a three-bucket Savonius rotor with a combined three-bucket Savonius–three-bladed Darrieus rotor*, 2008, Renewable energy

[8]   J. Jacob, D. Chatterjee, *Design methodology of hybrid turbine towards better extraction of wind energy*, 2019, Renewable Energy, vol. 131, pp. 625-643

[9]   A. Ahmedov, *Investigation of the Performance of a Hybrid Wind Turbine Darrieus-Savonius*, Abstract of PhD Thesis, 2016

[10]   T. Wakui, Y. Tanzawa, T. Hashizume, T.Nagao, *Hybrid configuration of Darrieus and Savonius rotors for stand-alone wind turbine-generator systems*, Electrical Engineering in Japan, p. 13-22, vol. 150, 2005

[11]   B. Molnar, *Comparison of structured and unstructured meshes for the computations of an H-type Darrieus wind turbine*, Final Thesis, Energetics engineering MSc, Faculty of Mechanical Engineering and Informatics University of Miskolc – Hungary and Institute of Fluid Dynamics & Thermodynamics "Otto von Guericke University Madgeburg" – Germany, 2014

[12]   I. Mălăel, V. Drăgan, G. Vizitiu, *The Vertical Axis Wind Turbine Efficiency Evaluation by Using the CFD Methods*, Applied Mechanics and Materials, Vol. 772, pp. 90-95, 2015

A SOLUTION FOR CH_4 LOSSES COMING FROM A MOTOR-COMPRESSOR EVACUATION

Andreea MANGRA[1]

ABSTRACT: Methane is a powerful greenhouses gas with a global warming potential 23 times that of CO_2 . Research has been conducted in order to design a device which can be mounted on an existent motor-compressor assembly intended for use in natural gas compression stations. The novelty consists in a concept based on ejection phenomenon which assure aspiration of CH_4 by an engine exhausted gases system. In order to observe if the device captures the CH_4 losses and if they are sucked through the pipe due to the ejection phenomenon a numerical simulation has been conducted using the commercial software ANSYS CFX.

KEYWORDS: CH_4, motor-compressor, CFD, ejection, pollution reduction

1. INTRODUCTION

Methane is a powerful greenhouses gas with a global warming potential 23 times that of CO_2 [1]. About 60% of global methane emissions are due to human activities [2]. The main sources of methane emissions are the oil and gas industries, agriculture, landfills, wastewater treatment, and emissions from coal mines.

Methane is the primary component of natural gas, with some emitted to the atmosphere during its production, processing, storage, transmission, distribution, and use. It is estimated that around 3% [2] of total worldwide natural gas production is lost annually to venting, leakage, and flaring, resulting in substantial economic and environmental costs.

The US Environmental Protection Agency (EPA) estimates that the natural gas system contributed about 23 % of annual US methane emissions in 2012 [3]. The 2012 EPA Greenhouse Gas Inventory atributes one-third of methane emissions from the US natural gas system to the transmission and storage sector.

Methane emissions from gas operations represented 6% of the total EU methane emissions, equivalent to 0.6% of the total EU GreenHouseGases emissions in 2016 [4].

While in past years, regulations have primarily targeted emissions generated from combustion processes and blowdown activities, fugitive emissions from compressor stations are becoming more and more of a concern. Fugitive emissions result from methane that leaks unintentionally from naatural gas station equipment or components [4].

One source of CH_4 fugitive emissions is represented by the CH_4 losses coming from the compressors used in natural gas compression stations. Seals installed around the rotating shaft are used to prevent process gas (methane) from escaping where the shaft exits the compressor casing. Wet seals, which use circulating oil as a barrier, were used extensively from the 1960s to the 1990s [5]. However, most compressors in operation today feature dry gas seals (DGS). The most widely used for natural gas applications is a tandem design. During compressor operation, the primary seal absorbs the pressure differential. The secondary seal serves as a backup in the event of primary seal failure. Though DGS systems are highly effective, small volumes of methane leak across the primary seal and vent to the atmosphere [5].

---

[1] Romanian Research and Development Institute for Gas Turbines COMOTI, Bucharest, Romania

Research has been conducted in order to design a device which can be mounted on an existent motor-compressor assembly intended for use in natural gas compression stations. The novelty consists in a concept based on ejection phenomenon which assures aspiration of CH$_4$ emissions by an engine exhaust gases system.

A sensor is currently being used to detect the CH$_4$ losses. When the accumulation of CH$_4$ emissions in the respective area of the motor-compressor assembly exceeds a certain level recorded by the sensor, the assembly is switched off automatically. The disadvantage of this technical solution is that the sensor has a minimum level of CH$_4$ emissions that it can detect and thus the amounts of CH$_4$ lower than this threshold is lost in the atmosphere. The sensor's accuracy level is +/- 3% of LEL (lower explosive limit) CH$_4$ or +/- 5% of the measurement [6].

Installing ejectors on compressor blowdown vent lines for reducing emissions when taking compressor off-line is a sollution presented by [7]. The ejector can be installed on vent connections up and down stream of a partly closed valve, or between the discharge and suction of a compressor which creates the necessary pressure differential. The captured gas and the motive gas are then routed to compressor suction or fuel gas system. Siemens also proposes an ejector concept for "sucking" and recompressing fugitive emissions [5]. The recompressed gas can then be reinjected into any number of operational processes, including the compressor inlet and the fuel system inlet.

The proposed concept (Fig. 1) consists of a funnel (1), which is fixed on the compressor casing, above the driving shaft, in the area where CH$_4$ losses may occur; a nozzle (3) that is mounted on the exhaust drum of the thermal engine that drives the compressor and a pipe (2) that connects the funnel and the nozzle. The CH$_4$ emissions are sucked using the ejection phenomenon through a pipe that is introduced into the flue gas flow resulting from the thermal engine driving the compressor and burned (Fig. 2). The nozzle is designed in such a way its diameter is higher than the exhaust drum diameter so that the presence of the pipe in the exhaust gas flow will not affect the proper functioning of the thermal engine.
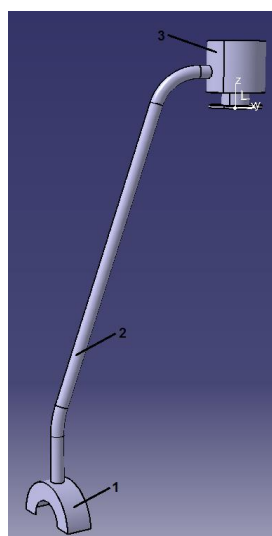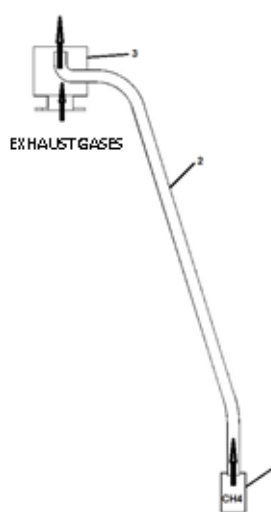
Fig. 1 The device   **Fig. 2 Section through the device**

The proposed concept has been designed starting from an existent moto-compressor assembly (Fig. 3), which is equiped with a CATERPILLAR thermal engine. According to the engine's specifications the exhaust gas temperature is of 548°C [8]. Over the years values in the interval 537°C - 670°C[9,10,11,12] have been reported for the methane auto-ignition temperature. The device can be addapted so it can be mounted on other moto-compressor assemblies, equiped with thermal engines with higher exhaust gas temperatures in order to be sure that the used natural gas auto-ignition temperature is reached. In the cases in which the auto-ignition temperature is not ensured, and thus combustion will not occur, the proposed device will ensure the disposal of the CH$_4$ emissions away from the moto-compressor assembly. Thus it will be avoided the formation of an explosive atmosphere.

The proposed solution is suitable for gas wells where the gas deposit pressure no longer ensures the operation and a moto-compressor is needed to increase the gas pressure for injection in the main gas network.

Fig. 3 The device mounted on the moto-compressor assembly

The device has the following advantages:

1. Technical advantages:
- the device has a simple design, which leads to its easy realization
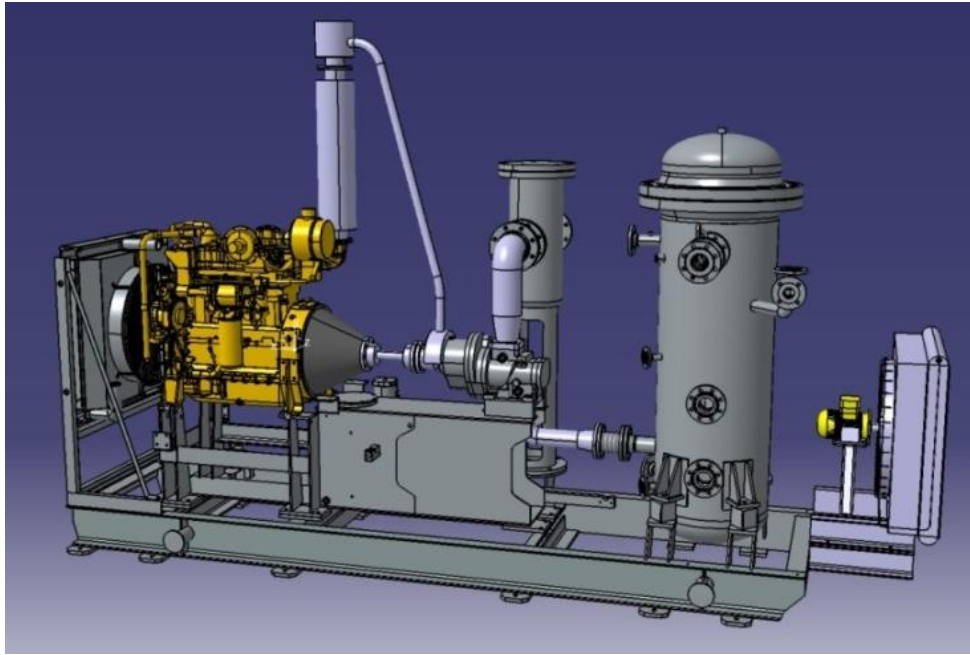- has no moving components
- does not require a dedicated power source for operation
- does not require special materials
- is easy to assemble

2. Economical advantages:
- the simple device design reduces material consumption and labor hours
- requires cheap materials
- provides conditions for the commanded shutdown of the motor-compressor

3. Ecological advantages:
- ensures the avoidance of uncontrolled accumulation of CH_4 and the formation of explosive air-CH_4 mixtures
- by burning these CH_4 losses, it contributes to the decrease of global warming, because the elimination of CH_4 in the atmosphere is 23 times more dangerous than the CO_2 resulting from its burning [1].

2. CFD SIMULATION

In order to observe if the device captures the CH_4 losses and if they are sucked through the pipe due to the ejection phenomenon a numerical simulation has been conducted using the commercial software ANSYS CFX. A simplified computational domain (Fig. 4), including the thermal engine outlet, the compressor driving shaft area of interest and the device designed to evacuate the CH_4 losses, has been used in order to reduce the computational time.

a)   b)
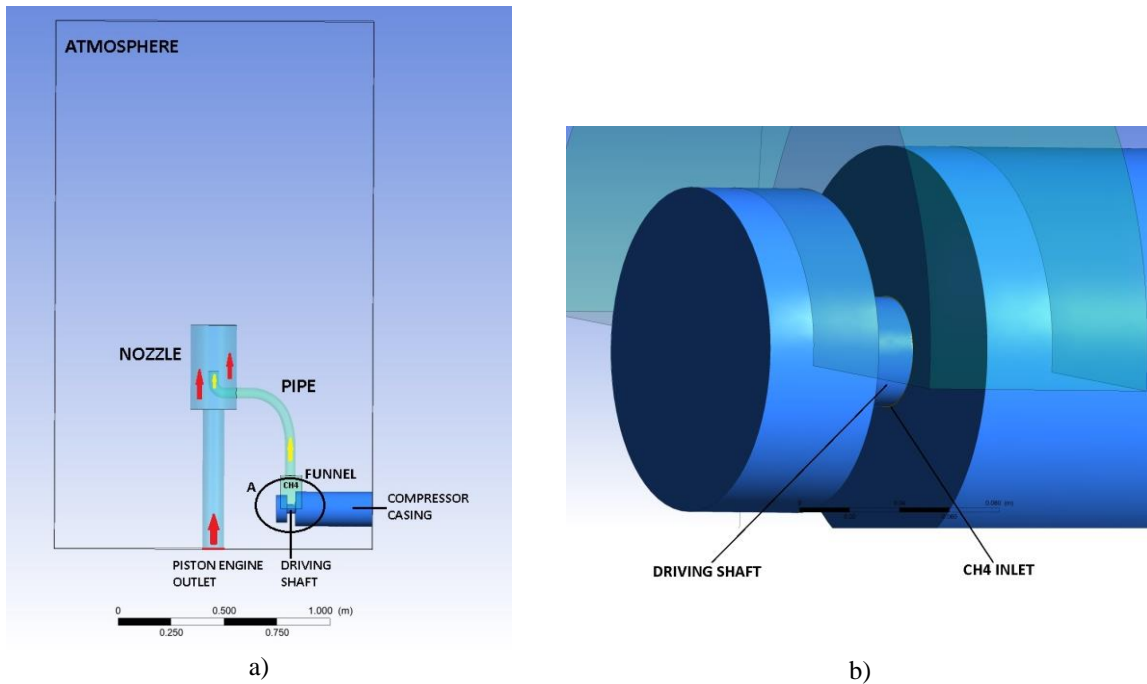
Fig. 4 a) Computational domain b) Detail A

The computational mesh has been generated using ICEM CFD. The mesh is of unstructured type. It has 5.905.686 elements and 988.043 nodes. The mesh is more refined in the funnel area and along the pipe and the thermal engine's exhaust (Fig. 5).
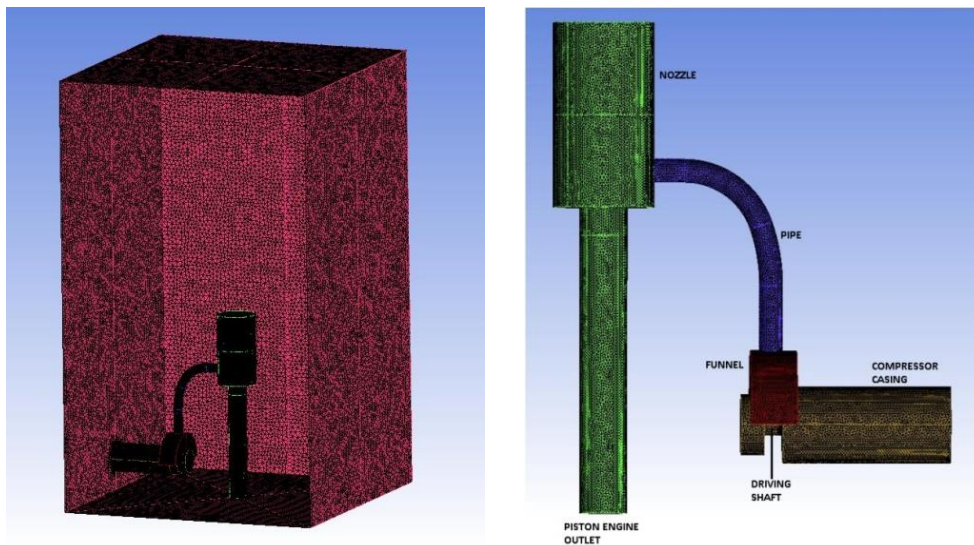
Fig. 5 The computational mesh

A RANS type turbulence model has been chosen, namely, the k-ε model (5% turbulence intensity), which is a numerically stable and robust model and very popular in the realization of technical applications numerical simulations. The reference pressure has been set to 1 bar. Buoyance has been taken into consideration. The reference density has been set at 1.2 kg/m^3. The boundary conditions are presented in Table 1. The conditions at the thermal engine outlet have been set according to the engine's functioning specifications [8]. In [8] are specified an exhaust gas flow rate of 13 m^3/min and an exhaust temperature of 548 °C. Knowing the exit section of the thermal engine exhaust drum it resulted an exhaust gas velocity of 27.5 m/s. A small value for the methan gas velocity has been imposed (0.1 m/s) because the case of small leakeages of methan gas, that can not be detected by the sensor, is investigated.

Given that at this stage it is investigation only the flow through the proposed device, not the burning of the CH_4 losses, to further simplify the simulation, it has been considered that through the thermal engine outlet enters the computational domain air and not exhaust gases.

Table 1. Boundary conditions

Boundary	Imposed condition
Thermal engine outlet	Normal speed 27.5 m/s, total temperature 548 °C [8], air mass fraction 1
CH_4 inlet	Normal speed 0.1 m/s, total temperature 120°C, CH_4 mass fraction 1
Atmosphere	Opening relative pressure 0 bar, opening temperature 20°C, air mass fraction 1
Walls	No slip wall, smooth, adiabatic

3. CFD SIMULATION RESULTS

In Fig. 6 are presented the velocity vectors on a longitudinal plan through the motor exhaust nozzle and the proposed device.
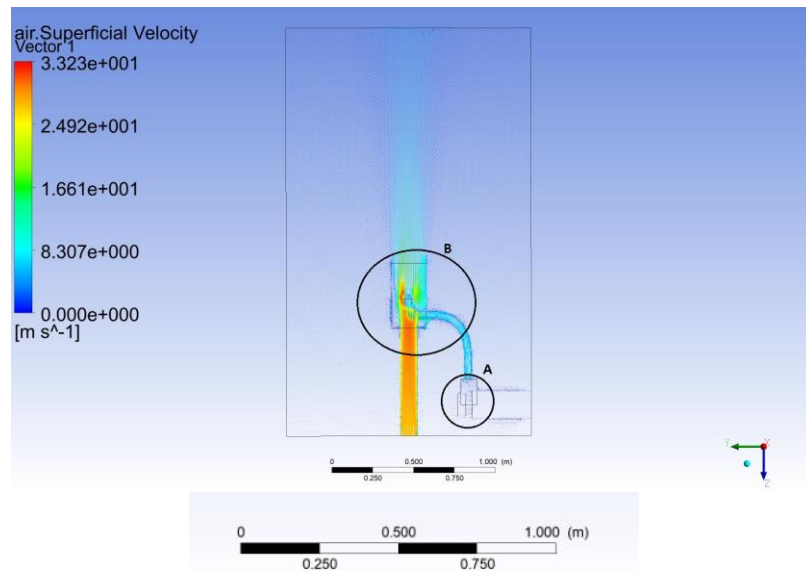

Fig. 6 Velocity vectors

Given the big difference between the velocities in the thermal engine nozzle in comparison with the velocities in the funnel and pipe, detail A (Fig. 7) and detail B (Fig. 8) have been created to better observe the velocity vectors direction.
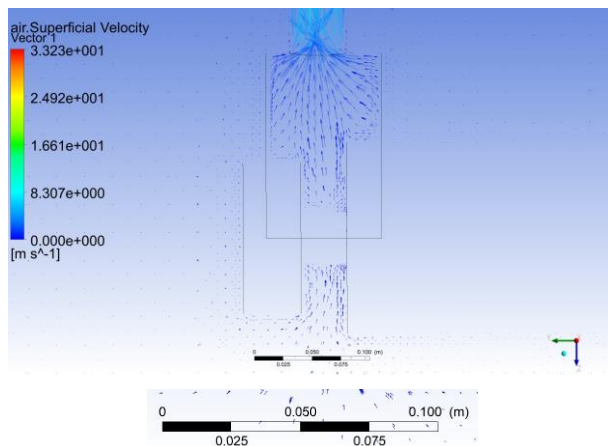
Fig. 7 Detail A Velocity
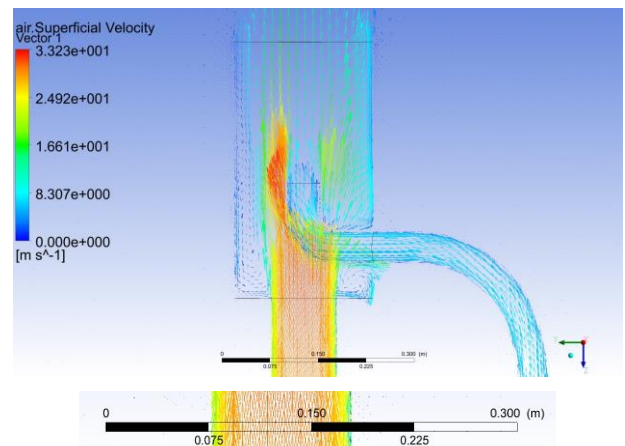
Fig. 8 Detail B Velocity

18

The velocity vectors directions confirm that, due to the ejection phenomenon, the CH$_4$ losses are sucked through the pipe.

In Fig. 9 is presented the CH$_4$ volume fraction filed on a longitudinal plan passing through the proposed device and the thermal engine exhaust nozzle. Because the CH$_4$ volume fraction is very small in comparison with the air volume fraction, the CH$_4$ volume fraction values interval has been changed from 0 to 1 to 0 to 0.001. Thus it can be observed that the CH$_4$ losses are sucked through the pipe.
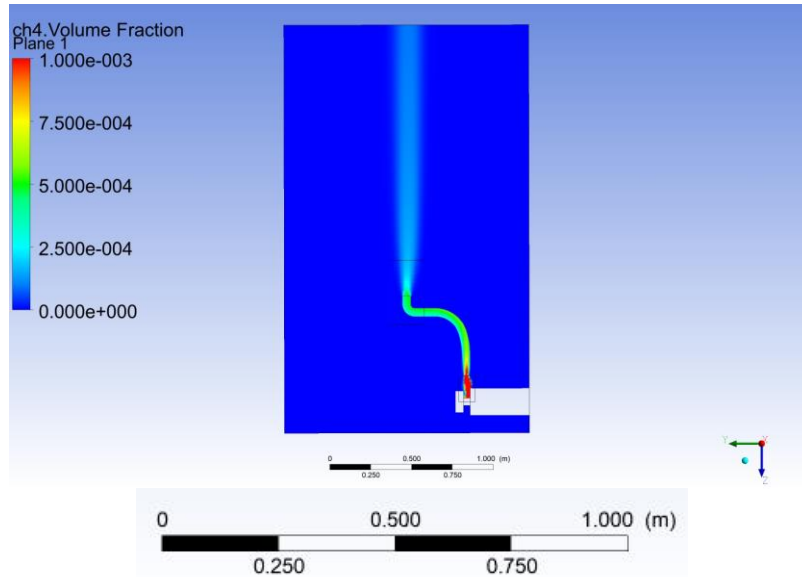
Fig. 9 CH$_4$ volume fraction field

Two surfaces have been created in order to verify if all the CH$_4$ emissions are sucked through the pipe due to the ejection phenomenon. One surface has been created at the pipe's end situate in the nozzle (Surface 1), and the other surface has been created at the nozzle exit (Surface 2) (Fig. 10).
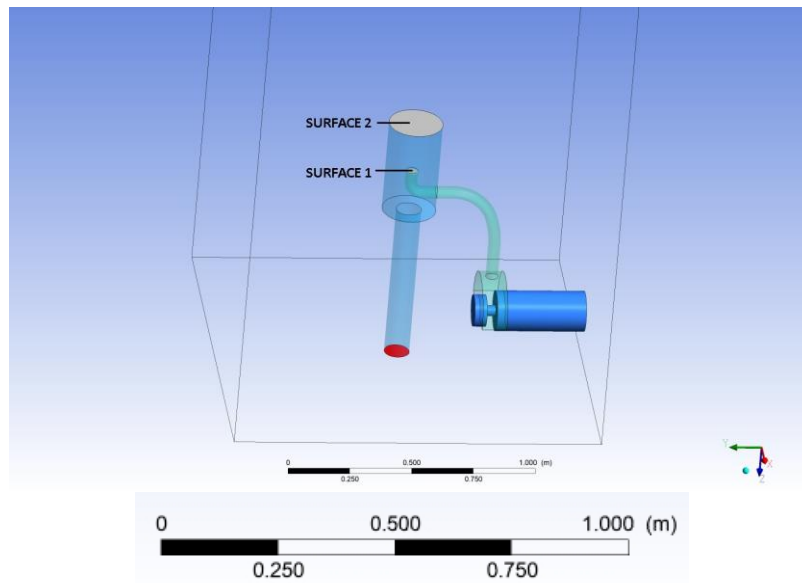
Fig. 10 Control surfaces positioning

In fig11, respectively fig. 12, is presented the CH4 volume fraction field on Surface 2, respectively the CH4 velocity on Surface 2.
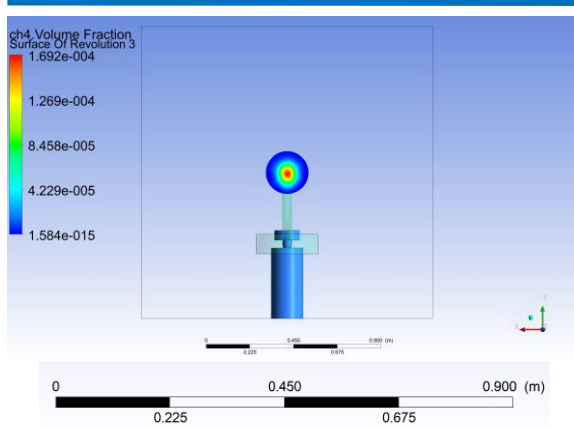
Fig. 11 CH$_4$ volume fraction field
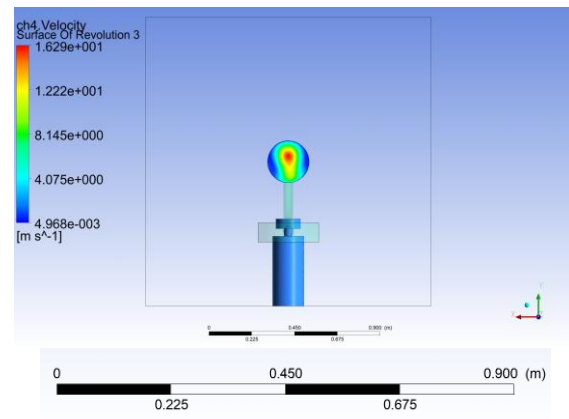
Fig. 12 CH$_4$ velocity field

Table 2. Mass flow through the proposed device

Section	Mass flow (kg/s)	
	Air	**CH$_4$**
Thermal engine outlet	0.0963	0
CH$_4$ inlet	0	3.5*10^-6
Surface 1	0.0154	3.5*10^-6
Surface 2	0.1117	3.5*10^-6

The numerical simulations results presented in Table 2 prove the proposed device efficiency. All CH$_4$ emissions are sucked through the pipe due to the ejection phenomenon.

The minimum quantity of air (minL)necessary for CH$_4$ to burn is 17.1 kg air to 1 kg CH$_4$. Thus, for 3.5*10^-6 kg of CH$_4$ minL=0.00006 kg air. Based on the results presented in Table 2, the existent quantity of air is much higher then minL. Thus, if the CH4 auto-ignition temperature is reached, there is enough air to ensure the CH$_4$ emissions burning.

4. CONCLUSIONS

A new device has been designed in order to evacuate the CH$_4$ losses from the motor-compressor assembly area in a simple, safe and less expensive way.

In order to verify the functioning principle of the device a numerical simulation has been conducted using the commercial software ANSYS CFX. The results confirm that, due to the ejection phenomenon, the CH$_4$ losses are sucked through the pipe connecting the funnel with the nozzle mounted on the thermal engine evacuation.

The device can be addapted so it can be mounted on any moto-compressor assemblies, equiped with thermal engines. The exhaust gas temperature has to be checked. This has to be equal or higher than CH$_4$ auto-ignition temperature for the sucked CH$_4$ emissions to be burned. In the cases in which the auto-ignition temperature is not ensured, and thus combustion will not occur, the proposed device will ensure the disposal of the CH$_4$ emissions away from the moto-compressor assembly. Thus it will be avoided the formation of an explosive atmosphere.

The presented device is the subject of the patent application nr. A/00016 from 20.01.2021.

For future work, the numerical simulations will include the burning of the CH4 losses in the thermal engine exhaust nozzle. The numerical results will be validated through experiments.

REFERENCES

[1] Chen C., Greene N., Is landfill gas green energy?, Natural Resources Defense Council, March 2003
[2] www.unece.org/challenge - accessed on 20.05.2021

[3] Subramanian R., Wiliams L., Vaughn T. et al., Methane Emissions from Natural Gas Compressor Stations in the Transmission and Storage Sector: Measurements and Comparisons with the EPA Greenhouse Gas Reporting Program Protocol, Environmental Science & Technology, vol. 49, pp. 3252-3261, 2015

[4] GIE & MARCOGAZ, Potential ways the gas industry can contribute to the reduction of methane emissions, Report for the Madrid Froum, 5-6 June 2019

[5] Chhibber G., Bacui S., Methods for reducing fugitive emissions from natural gas compression stations, COMPRESSORTECH, 2020

[6] Infrared Detector for FlammableGases, Technical Manual, type OLCT IR E, OLDHAM

[7] Reducing Emissions When Taking Compressors Off-Line, Environmental Protection Agency (EPA), U.S.A., 2006

[8] CATERPILLAR G3304 Gas Petroleum Engine (71 bkW), Engine specifications, CATERPILLAR, 2009

[9] Bounaceur R., Glaude P., Sirjean B., Fournet R., Montagne P., Vierling M., Moliere M., Prediction of auto-ignition temperatures and delays for gas turbine applications, Journal of Engineering for Gas Turbines and Power, vol. 138, pp. 021502, 2016

[10] Kundu S., Zanganeh J., Moghtaderi B., A review on understanding explosions from methane-air mixture, Journal of Loss Prevention in the Process Industries, vol. 40, pp. 507-523, 2016

[11] Cristescu T., Stoicescu M., Stoianovici D., Argumente cu privire la utilizarea gazelor natural lichefiate, Conferinta Nationala de Termotehnica, 2017

[12] Fisa cu date de Securitate Gaz Natural, Societatea Nationala de Gaze Naturale Romgaz S.A., 2012 2009

CENTRIFUGAL PUMP BREADBOARD DESIGN FOR A MECHANICALLY PUMPED FLUID LOOP COOLING SYSTEM

Ionuț-Florian POPA[1], Gheorghe MEGHERELU[1], Radu MIHALACHE[1], Dragoș MIHAI[1], Alexandra ADIACONIȚEI[1], Emil NUȚU[1], Virgil STANCIU[2]

ABSTRACT: At international level there is a high demand of active thermal control systems (ATCS) for spacecraft, as these are more efficient than the classic solutions, such as thermal insulation or passive radiators. One of these systems is the Mechanically Pumped Fluid Loop, which uses liquid in order to transport and reject the heat generated by the onboard systems. Qualified pumps for space are produced currently in USA, thus the development of such a pump in Europe could lead to ensuring the continent's independency in this regard. The current paper addresses to the design of a centrifugal pump as part of a Mechanically Pumped Fluid Loops (MPFL) for spacecraft thermal control. Key aspects of these systems are highlighted and their influence over the design of the pump is described. Several design features important for an MPFL pump are pursued such as driving requirements, common problems of such equipment (working fluids, hydraulic design, lubrication, thrust balancing) and optimization aspects like the use of trade-offs to select the most suitable materials, configurations and technologies appropriate for this type of equipment. In the end of the paper a development plan is suggested along with a series of tests necessary to validate and qualify the product. The proposed design targets an operating lifetime up to 15 years.

KEYWORDS: centrifugal pump, mechanically pumped fluid loop, impeller, thrust balancing, canned motor pump

1. INTRODUCTION

The spacecraft thermal control system is an important part of the nowadays large space platforms, as they have to deal with high temperature differences between two opposite sides, fact which may affect the overall functioning of the systems onboard. Moreover, the new generation of spacecraft has increasingly complex payloads, thus resulting in an increased power consumption which generates high heat fluxes. The heat must be either dissipated or transported to another payload needing heat in order to function properly. There are several types of different active and passive systems which can be successfully applied in this domain, one of the most common systems being the fluid loop system where a liquid coolant is circulated in a closed loop under the action of a pump (Fig. 1).

---

[1] Romanian Research and Development Institute for Gas Turbines COMOTI, Bucharest, Romania;
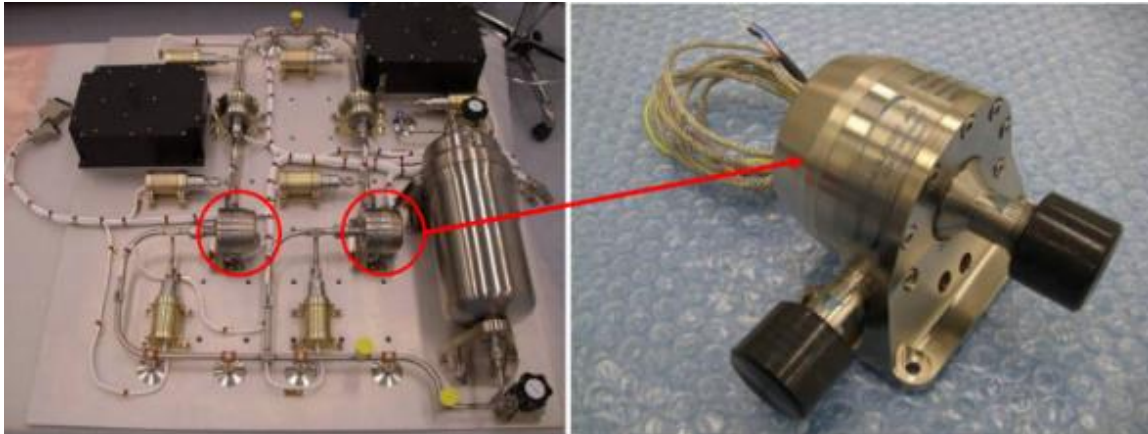[2] „Politehnica" University of Bucharest, Bucharest, Romania.

Fig. 1. Mechanically Pumped Fluid Loop developed by Real Technology AG [1]

The most important part of a mechanically pumped fluid loop is the pump. Usually centrifugal, the pump ensures the flow of the cooling liquid through the closed loop. Its functioning is essential for the proper operation of the spacecraft systems.

The development of a new and improved centrifugal pump for mechanically pumped fluid loops is of high interest for the European space industry. The study and development of space-qualified mechanical pumps for fluid loops started at ESA in the late 1970s [2]. This domain was pursued also by NASA or JAXA in the following years.

Pumps for such applications come in different shapes and sizes, depending mostly of the flow rate they shall ensure and the pressure rise needed. Given the necessity of ensuring the lubrication and cooling of the pump assembly, most of the architectures developed in the past are canned type, having the electric motor integrated with the pump's housing. One of the first architectures of this type was designed for the Columbus module which is part of the International Space Station. According to ref. [3], the pump ensures a flow rate between 100 and 850 kg/h, with a pressure rise up to 4 bar, using water as working fluid.

Mechanically Pumped Fluid Loop systems can be of two types, Single-Phase MPFLs and Two-Phase MPFLs. Of interest for the current paper are the Single-Phase ones. The difference between them is that in the single phase loop the working fluid is always in liquid state while in the case of the two-phase loop the liquid passing through the pump is moved in the high temperature area where it evaporates, absorbs the heat and then moves to the area where the heat is radiated, determining the working fluid to condensate entirely and back as liquid. The main characteristic of a MPFL is its heat load rejection, usually ranging between 1 and 20 kW. Usually, the pump works at a constant flow in order to have an in-service life as long as possible.
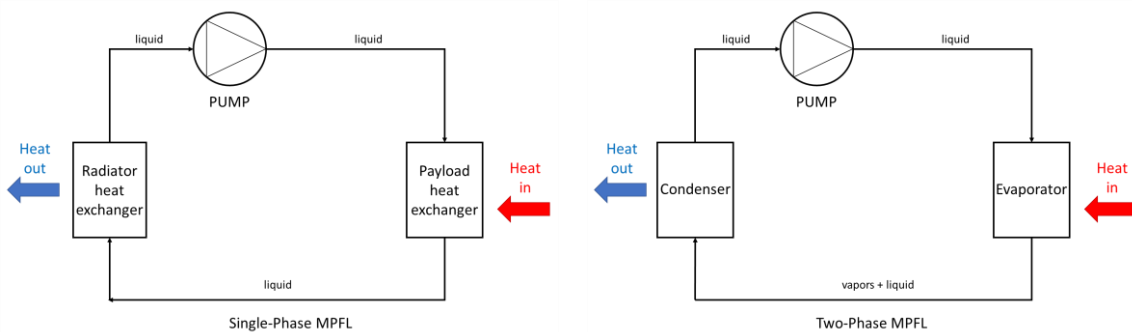
Fig. 2. Single and Two Phase Mechanically Pumped Fluid Loop

Another important aspect for the MPFL system and the pump is the fluid used. The heat transport is made with specialized fluids such as water/polypropylene mixture, HFE 7200 or Galden. There is also the intention to use ammonia in the MPFL, as it ensures the best performances in this type of systems when it comes to heat transport [4]. However, there are several issues and risks associated with ammonia, such as the compatibility with the materials used (i.e. copper, a material with excellent heat transport properties reacts

with ammonia [5]), toxicity for the operators [6] and the most stringent one, its vaporization. Ammonia has a low vapor pressure; therefore, it has to be kept all times at very high pressures. In some areas or points along the loop, the temperature can be higher than the operating temperature of the MPFL system, reaching as high as 70°C. At this temperature, the minimum pressure inside the MPFL system shall be higher than 40 bara, in order to prevent the ammonia from evaporating in the system. This pressure imposes that the MPFL shall be very robust, with thick walls for the pump casing, piping, accumulators, heat exchangers and so on.

Fig. 3. Ammonia effects over copper [5]

A suitable pump for ammonia was designed in the past based on the Columbus module requirements presented before. Wunderlich et al. [7] proposed a pump design having the inlet and outlet at different ends, suggesting a cooling of the pump assembly through its length. Following the tests a 8.5 l/min flow rate was obtained at 7500 rpm, both for water and ammonia. The pump architecture and the produced prototype are presented in **Fig. 4**.
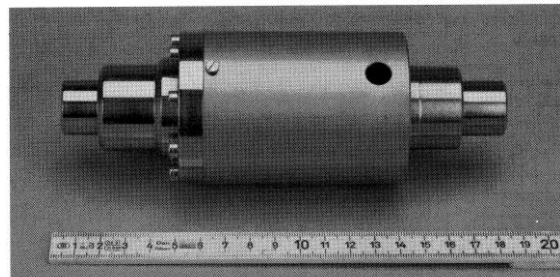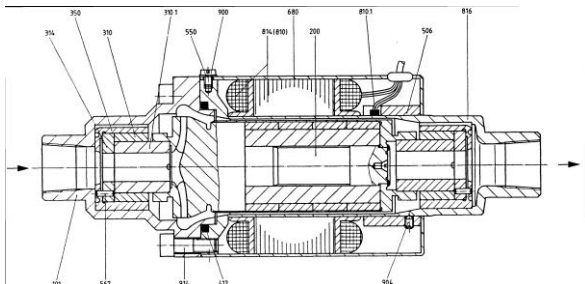
Fig. 4. Ammonia pump based on Columbus specifications [7]

In the 2000s Pacific Design Technologies developed two mechanical pumps for the Mars Science Laboratory [8][9], as part of the Mars Exploration Program coordinated by NASA. These pumps are designed to operate with either CFC-11 or water, being still active on the Curiosity rover which is studying Mars in search of potential life signs from the past or present [10].
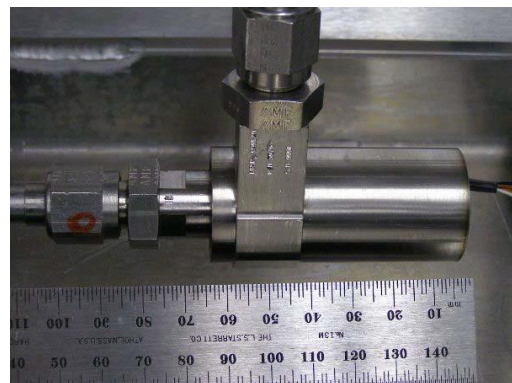
Fig. 5. Mars Science Laborabory pumps (left – MSL Engineering High Flow Water Pump, right – MSL Rover Engineering Pump) [8]

At this moment, at European level there are several projects under implementation regarding the development and qualification of centrifugal, gear pumps or piezo electric membranes. As their development is still in early stages, the European space missions are equipped with pumps produced outside of Europe, but this usually implies higher costs or other kinds of risks. One of the main companies developing such products is former Realtechnologie AG, currently known as nanoSPACE, which is developing a family of pumps for space applications [11].

Fig. 6. Family of pumps currently under development by nanoSPACE, former Realtechnologie AG [11]

Depending on the application, the pumps for MPFL systems usually ensure mass flow rate values between 300 and 1500 kg/h at inlet pressures ranging from 1 to 7 bara. Another important parameter of the pump assembly is the power consumption of the electric motor used to drive the pump. The power consumption is proportional to the mass flow (the higher the mass flow, the higher the power consumption), ranging between 80 and 500 watts. All these performances are related to the type of fluid used for the MPFL system. For the same pump, different working fluids and duty points mean different performances. For a space platform using more than one MPFL and cooling fluids, different pumps shall be used, designed according to the requirements of each MPFL systems. This leads to the need of a family of pumps, meaning higher costs for the space industry. Thus, the ideal case presumes having a pump which can cover as many duty points as possible, while being compatible to several working fluids relevant for the application. An example is the future space platform I-HAB which is intended to be inhabited by people. The platform would use MPFL systems inside and outside, and the purpose is to use a single pump which can work with multiple working fluids at multiple duty points (on the inside only non-toxic working fluids shall be used).

The purpose of the presented work is to deliver in the near future a reliable pump assembly, which can cover a large domain of mass flow rates than the current existing alternatives, with the possibility to use such an assembly also for second markets (i.e. medicine). National Research and Development Institute for Gas Turbines COMOTI is implementing the project "*Centrifugal pump breadboard for a Mechanically Pumped Fluid Loop Cooling System*", financed by ESA under the Romanian Incentive Scheme, having the objective to develop a pump for an MPFL system.

2. PUMP GENERAL ARCHITECTURE AND PERFORMANCES

The architecture of a pump assembly for MPFL systems is defined by a set of requirements specific for the mission in which the system shall be integrated. Some of the most important requirements which will serve as a baseline for the design to be presented later in the paper are stated below:
- Pump assembly type: centrifugal, canned motor type (with integrated electric motor);
- Electric motor type: brushless, DC, foreseen with hydrodynamic bearings;
- Lifetime: between 4 and 15 years, depending on the application;
- Fluid compatibility: the fluids are mainly the ones specified before, namely water/propylene glycol mixture, HFE7200, Galden;

- Pump cooling: using internal by-pass circuits and a small mass flow of working fluid from the MPFL system;
- A hydraulic balancing device is needed;
- Mechanical loads: mechanical environment during launch and micro vibrations induced in operation;
- Raised pressure: 2 to 7 bara;
- Operational working fluid temperatures: for applications outside the spacecraft can be -40°C to +60°C (assuming that the freezing temperature of the working fluid is above the minimum operational temperature) and for applications inside the spacecraft it ranges between -10°C and + 50°C;
- Non-operational working fluid temperatures: usually 10°C to 20°C more severe than operational working fluid temperatures;
- Cosmic radiation: different levels depending on the application.

Based on these driving requirements and additional ones, a preliminary pump architecture is proposed below, corresponding to an engineering model phase. The assembly presented in Fig. 7 features two main subassemblies, the hydraulic part of the pump with its casing and the canned electric motor. As it can be observed, the rotor is completely contained in a sealed mechanical assembly which holds the working fluid. This equipment is completed by an Electronic Control Unit which facilitates the start, stop and operation of the pump at constant rotation speed for several duty points, but this is not shown and doesn't make the subject of the current paper.

At this stage of the pump (engineering model), the design features O-ring seals (double barrier) which allow the dismount of the EM pump between tests in order to inspect the parts. It is known the fact the O-rings lose their properties in time, thus for the next step (QM/FM) the intention is to use a permanent welding joint. Fig. 8 shows the main components of the preliminary pump assembly. As the development goes on, the components design will be optimized.
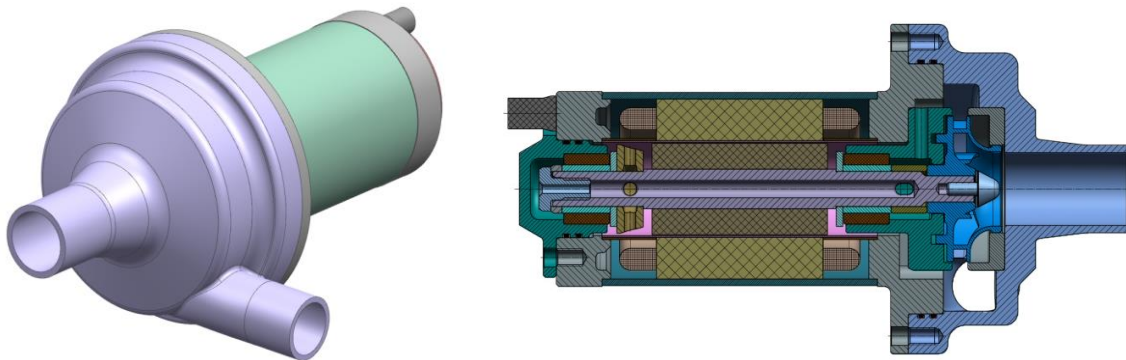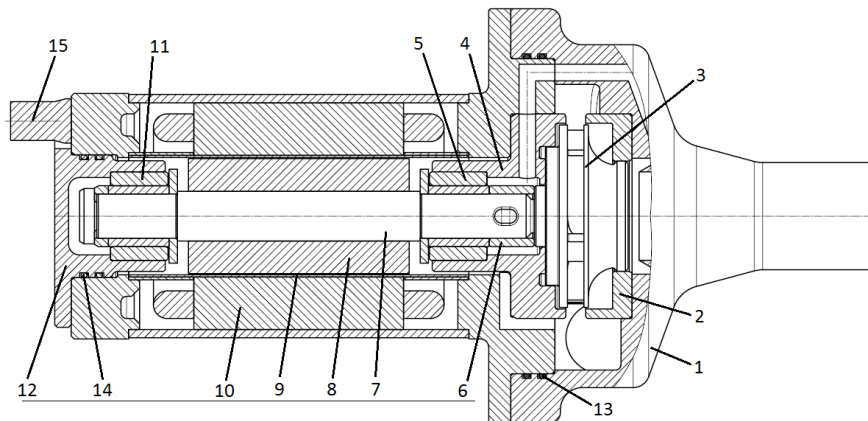

Fig. 7. MPFL pump assembly – CAD model view and section

1 – pump casing, 2 – inlet sleeve, 3 – closed impeller, 4 – front support bearing, 5 – front bearing, 6 – spacer, 7 – shaft, 8 – rotor core, 9 – stator liner, 10 – stator core, 11 – rear bearing, 12 – rear support bearing, 13, 14 – O-rings, 15 – terminal electric cables

Fig. 8. MPFL pump assembly – main components

Several of the components are critical for the proper functioning of the pump assembly. These components are optimized through an iterative process using CFD and FEM tools. The optimizing process will consider the following aspects:

- Optimization of the flow channel geometry through which the working fluid is passing along with the radial and axial clearances of the system meant to ensure the impeller's position – areas A1 and A2 from Fig. 9 left side, using theoretical and CFD analysis;
- Optimization of the secondary flow for the axial thrust balancing of the impeller with minimum impact over the efficiency of the pump – area B from Fig. 9 right side, theoretical and CFD analysis;
- Dimensioning of the rotor cooling circuit through the electric motor and bearings, including the impeller from the back of the motor shaft – establish the dimension of the nozzle through which the working fluid is circulating, along with the minimum flow rate necessary to ensure the appropriate cooling of the electric motor and bearings;
- Hydraulic characteristics calculus: flow rate, pressure, speed, total head – based on the obtained information, a pump performance map can be generated;
- Rotor and bearing dynamics – the rotor will be optimized using FEM analysis taking into account the mechanical loads during operation, such as launch loads (vibration, sine, shock) and micro vibrations occurred in functioning;
- Pump's casing ability to withstand the working pressures – this is validated both theoretically and using FEM analysis.
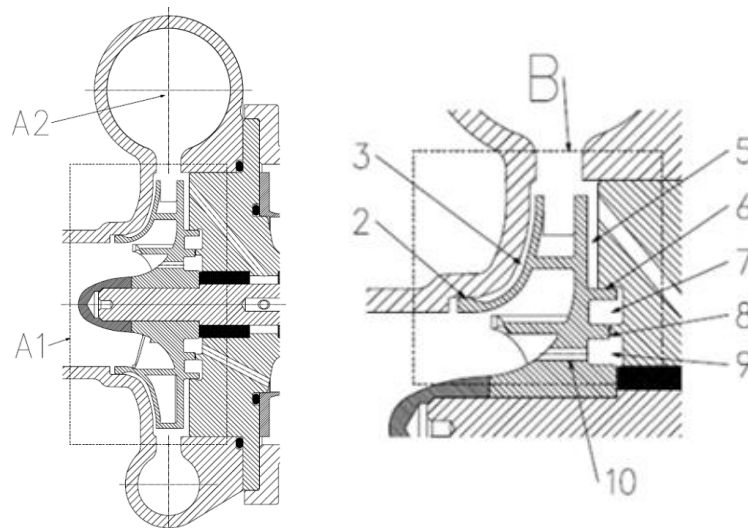
Fig. 9. Typical areas of a pump assembly to be approached in the CFD optimization, left side – main flow, right side – secondary flow for axial thrust balancing
2 – front gap (radial shape), 3 – front shroud cavity, 5 – back shroud cavity, 6 – back gap (radial shape), 7 – balance cavity, 8 – balance gap (axial type), 9 – back hub cavity, 10 – balance holes

One of the most important aspects in the pump's functioning is the appropriate lubrication of the bearings. The pump assembly is foreseen with two bearings, one in the front and one in the back. Given the operating conditions of the pump, the lubrication is hydrodynamic and it uses the working fluid, simplifying the design of the pump (no additional separate circuits and liquids for lubrication). As this is a sensitive subject, especially for the space industry, simple, but yet effective methods can be used to track the best solutions for the bearings of this type of equipment. Such a method is to perform a trade-off during the development phase. For the current subject a trade-off can be made regarding the bearing technology to be used. A possible configuration could be using a shaft coated with a hard layer of chrome oxide or another material. Also, an assessment shall be done between different types of materials used for sleeve bearings such as ceramic or sintered silicon carbide sleeves placed over the shaft. The lubrication circuit is dimensioned firstly by calculus to determine the necessary flow through the bearing system, and subsequently optimized through CFD to include also the temperature effects over the bearings.

As the operation period is extensive (up to 15 years), the pump needs a very precise mechanical dynamic balancing due to its size (up to class 0.4G according to [12]). The design has also a hydraulic balancing device, but these are discussed in the next paragraph which is dedicated to the hydraulic part of the pump.

3. PUMP HYDRAULIC PART DESIGN

The hydraulic part of the pump ensures the flow of the working fluid through the loop system by increasing the kinetic energy of the fluid which enters at the centre of the rotating impeller and moves to the outer diameter of the impeller. The centrifugal pump is not generating pressure, it only moves the liquid, allowing it to self-adapt in case of a hydraulic blockage for some time without needing a pressure limiter or an overflow valve.

The design of the pump hydraulic part features a closed centrifugal impeller, having 30 mm in diameter, with 6 backward curved blades. Also, the impeller is foreseen with two shrouds and a hub. The purpose of the front shroud is to eliminate the leakage losses across the blades, while providing strength and stability to the blade, given the high speed at which the impeller operates (between 10000 and 15000 rpm). This allows also a reduced thickness of the blade, increasing the flow area through the impeller. A CAD view of the impeller is presented in Fig. 10.
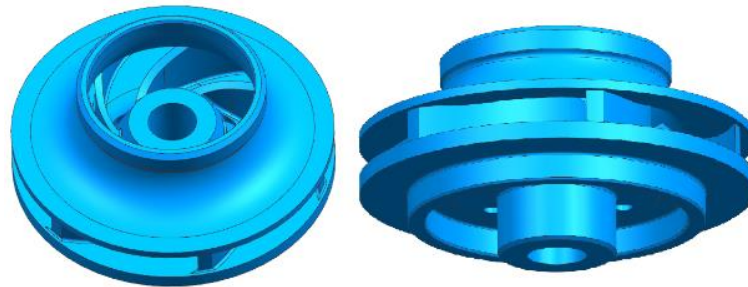
Fig. 10. Centrifugal impeller

Besides strength and stability, the two shrouds provide also an axial thrust balancing surface from which the pressure difference can be balanced. The axial thrust of the rotor is a central problem in the development of a hydraulic equipment and is generated by the impeller [13]. There are several methods to ensure the hydraulic balance of the rotor, the most common being the use of an impeller with holes which run into an axial gap on the back of the impeller (balance chamber).

The current impeller design is foreseen with an automatic thrust balancing device that performs to make the impeller self-standing in a certain balanced position through hydrodynamic action of the fixed and the variable orifices at the rear of the impeller. Even if this feature impacts the system in terms of efficiency (losses), it offers reliability to the to the pump, ensuring a long life of the bearings. A detail of the thrust balancing system is presented in Fig. 11.
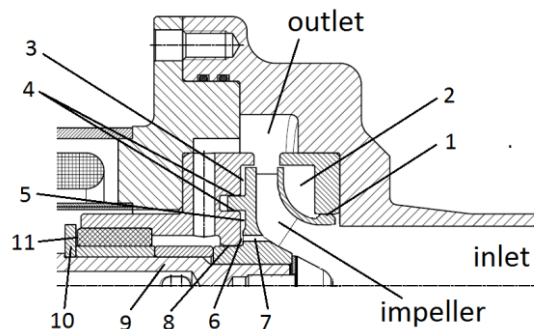
1 – front gap (fixed orifice), 2 – front shroud cavity, 3 – back shroud cavity, 4 – back gaps (fixed orifices), 5 – thrust balance chamber, 6 – balance gap (variable orifice), 7 – impeller holes, 8 – rear gap (fixed orifice), 9 – shaft, 10 – thrust bearings, 11 – gap in thrust bearing

Fig. 11. Thrust balancing device

As it can be seen above, the impeller has three holes (7) through the rear shroud near the hub, allowing the pressure at the balance camber to bleed through the holes (7) back into the suction area. Also, between the impeller and the body there is a chamber (5) where the working fluid enters through the radial gaps (4) and exits through the axial gap (6).

The rotor has an axial clearance between the sleeve bearings. When the pump is operating at steady state, the rotor remains in a fixed position because the axial forces acting on it cancel each other. In this position, the rotor has no contact with the sleeve bearings in the axial direction. When the pump is in operation and a disturbance occurs, the impeller moves axially, and a higher or lower pressure is created in cavity (5). The axial force created by this pressure in the cavity (5) returns the impeller to the neutral position. The balancing operation requires a certain amount of balancing flow through the clearance gaps (4) and (6) between the rotating and non-rotating parts. The pump has a hermetic construction, being foreseen with three working fluid circuits:

- The main circuit: between inlet and outlet (green);
- The circuit used to perform the hydraulic thrust balancing of the rotor (red);
- The circuit used to ensure the cooling and lubrication of the electric motor and bearings (blue).

A graphical representation of the three circuits through the pump is shown in **Fig. 12**:
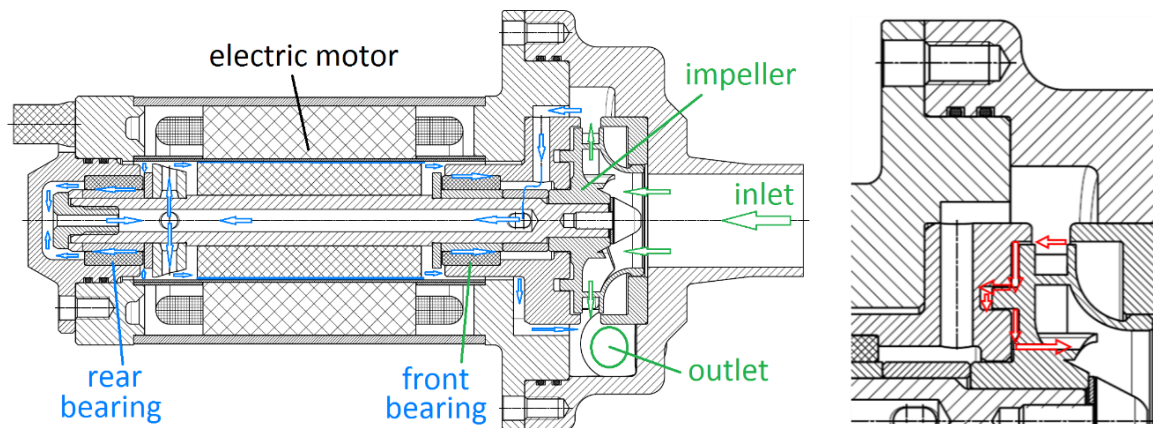

Fig. 12. Main and secondary flows through the pump assembly (left – main and lubrication circuit, right – detail on the thrust balancing circuit)

As it was mentioned before, the hydraulic thrust balancing circuit improves the operational life of the pump with very small consumption of working fluid, by-passing around 3% of the total flow of the pump. The cooling and lubrication circuit is more complex, as the working fluid has to get on all the length of the shaft and on the bearings. The flow is facilitated by adding an impeller on the back part of the rotor, ensuring a proper flow of the fluid back in the circuit. Depending on the dimensions of the pump, the flow estimated for electric motor and bearings cooling is approximatively 12% of the total flow of the pump. The flows for the two secondary circuits can be more precisely estimated by conducting design tests on a pump breadboard.

Some of the requirements dedicated to the hydraulic part of the pump influence also the design of the electric motor. This one has to operate as long as the pump and also, the materials used shall be compatible to the working fluid as it is used for cooling and lubrication.

Besides that, several typical requirements for an electric motor which shall work in space are:
- Canned type electric motor, DC brushless;
- Rotor with permanent magnets integrated on the shaft to have a solution as compact as possible (frameless motor);
- Choosing the suitable permanent magnets which shall maintain their properties for the entire lifetime;
- Minimum or none eddy currents which can influence the pump's functioning or the electronic equipment nearby;
- Electromagnetic compatibility with the spacecraft systems;
- Ability to withstand the pressure of the circuit, given that the electric motor bearings are cooled and lubricated using the working fluid.
- Radiation resistant.

4. PUMP DEVELOPMENT PLAN

Like in the case of any space product development, the purpose of testing is to demonstrate on ground, beyond doubt, the reliability of the equipment in conditions similar to the space environment. Furthermore, it shall be proved that the equipment is operational not just at a certain moment, but throughout the mission in which environmental conditions (temperature, vacuum, mechanical loads, radiation dose, etc.) may vary significantly. These tests are necessary not just at the end of the equipment assembly phase, but throughout the entire development process in order to demonstrate that the design is suitable to fly in space.

The final step in the pump's development is to subject it to an extensive testing campaign. The following tests are foreseen to be conducted at engineering level:

- Functional and performance tests: these types of tests are made throughout the entire development phase (design tests for the hydraulic part of the pump) and they shall be repeated after each environmental test (mechanical and thermal) to check if the pump operates accordingly; also, this test can include the burn-in test to check eventual problems during operation; for a more relevant testing, the temperature along the loop may be varied by adding different hot or cold sources;
- Mechanical testing: random and sinusoidal vibration, shock, corresponding either to the launching phase or to the vibrations induced by the pump while operating;
- Thermal vacuum test: these tests shall cover the thermal cycles occurred while the pump is operating in space; as in the case of the functional and performance tests, thermal loads can be added in the loop for a more relevant testing;
- Structural integrity: the ability of the casing to withstand the pressure inside the MPFL loop and to verify if there is any leakage on the pump.

The functional and performances tests will be carried out using a dedicated test bench. A schematic diagram of the test bench foreseen to be developed for the pump is shown in Fig. 13:
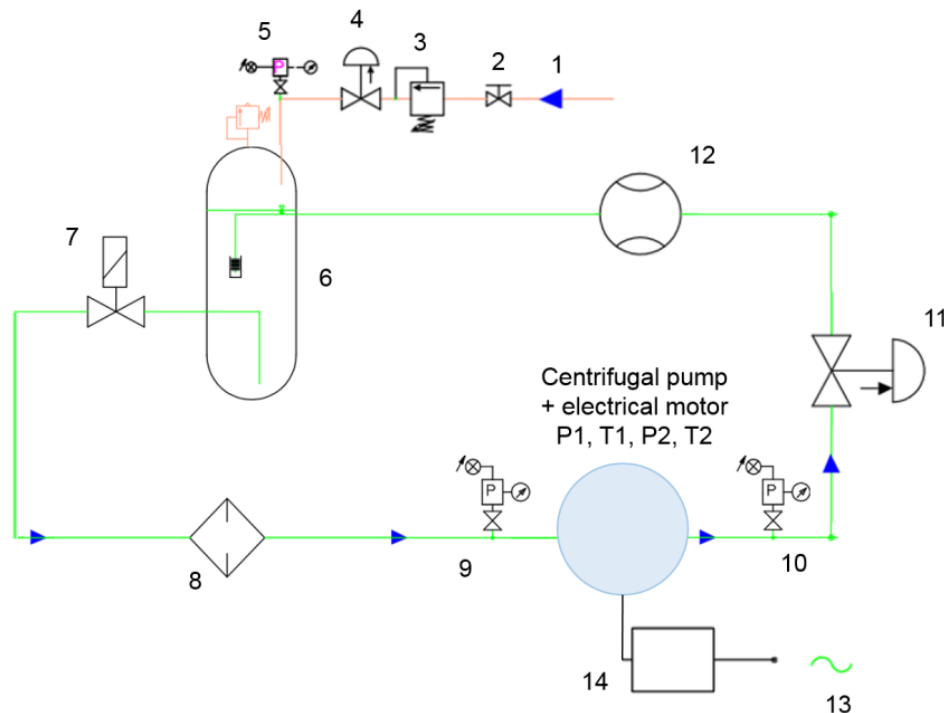
1 – compressed air source, 2 – isolation valve (closed/open), 3 – compressed air regulator, 4 – valve, 5 – connecting valve to the atmosphere, 6 – tank/accumulator, 7 – valve (closed/open), 8 – filter, 9, 10 – pressure gauge, 11 – flow control valve, 12 – flowmeter, 13 – electrical power source, 14 – Electronic Control Unit (ECU, not for space applications), 15 – differential pressure sensors (not represented), P1 – pressure sensor (front bearing), T1 – temperature sensor (front bearing), P2 – pressure sensor (rear bearing), T2 – temperature sensor (rear bearing), vibration sensors placed on the pump assembly casing, sensor for the rotation speed of the electric motor (not represented in the diagram above)

Fig. 13. Test bench – preliminary layout – to be used for EM performance tests

The test bench will be firstly used to conduct several design tests which will lead to the pump optimization, namely the impeller geometry. Its architecture includes a tank/accumulator, a system to pressurize the working fluid, different sensors to characterize and measure the impeller performances like pressure and temperature and an electric motor having similar performances to the one which will be featured on the pump assembly.

The next development phases of the pump will make use of the same test bench, but adapted to measure the pump assembly performances such as total head, pump capacity (rate flow), power input of the pump, rotational speed and so on.

The pump electric motor shall be able to withstand a minimum of 2500 on/off cycles. During this test the pump will have dynamic working regimes, with small flow rates and pressures. These flow rates cause a poor bearing lubrication, leading to pronounced wear. Also, the electric motor cooling is greatly diminished.

The testing of the pump's functioning is made in a wide range of flow rates and speeds lower or higher than the nominal ones in order to establish to what extent the pump can be integrated in other MPFL systems for other duty points. The purpose of these tests is to prove that the requirements are fulfilled. If there are issues found during the testing phase, a new iteration is performed to further optimize the design.

The design phases along with the testing campaign previously presented are associated to the development of the pump assembly engineering model (EM). The next phase of the project is to optimize the EM based on the test results to obtain a QM (qualification model) able to fully reflect all aspects of the flight model. The QM development phases include several major steps such as:
- review of the requirements according to the EM test results;
- final design and extensive analyses;
- QM manufacturing and testing.

Using the methodologies, procedures, processes and lessons learned from the EM and QM development, the next step is to develop the FM (flight model), to perform the acceptance tests in order to obtain a qualified product for space.

5. CONCLUSIONS

Pumps for Mechanically Pumped Fluid Loop systems are not new, but they are imperiously necessary as the space technologies nowadays imply more power, more heat and getting deeper in space. Also, manned missions will make use of these equipment to ensure habitability, either if we talk about lunar bases or operations in orbit.

In the current paper a centrifugal pump architecture is proposed having as a baseline a set of requirements from the Large Space Integrators, as well as Europe's needs for such thermal systems, given the fact that currently qualified pumps for MPFL systems are available only from USA. The pump design is a canned type one, with the electric motor connected to the pump's housing. The pump hydraulic part features a thrust balancing system capable of withstanding the axial loads which occur during the pump's functioning. Also, a cooling and lubrication circuit was designed and presented, targeting the fulfilment of the lifetime requirement, between 4 and 15 years, which is considered the most stringent one and it can be ensured by choosing the proper bearing system.

The future work will focus on defining the most suitable bearing solution for the pump, as well as improving the current design following CFD and FEM analyses.

ACKNOWLEDGEMENT

REFERENCES

[1]. *ESA's ARTES Programmes, Mechanically Pumped Fluid Loop,* https://artes.esa.int/projects/mechanically-pumped-fluid-loop;

[2]. van ES, J., van Gerner, H.J., van Bethem, R.C., Lapensee, S, Schwaller, D, (2016), Component Developments in Europe for Mechanically Pumped Fluid Loop Systems (MPLs) for Cooling Applications in Space, *46th International Conference on Environmental Systems*, Vienna, Austria;

[3]. Orlando R., Osella P., Ferrera M., Columbus Water Pump Package Overview, *21st International Conference on Environmental Systems*, San Francisco, California, July 15-18, 1991, SAE Technical Paper Series;

[4]. Karam, R., (1998), Satellite Thermal Control for Systems Engineers, *Progress in Astronautics and Aeronautics*, vol. 181, American Institute of Aeronautics and Astronautics, Virginia, USA;

[5]. Gilmore, D., (2002), *Spacecraft Thermal Control Handbook, 2nd edition*, The Aerospace Press, American Institute of Aeronautics and Astronautics, Virginia, USA;

[6]. Bruckner, R., Manco, R., (2014), ISS Ammonia Pump Failure, Recovery and Lesson Learned – A Hydrodynamic Bearing Perspective, *42nd Aerospace Mechanism Symposium*;

[7]. Wunderlich E., Wulz H.G., A Space Pump Prototype Designed for Operation in Thermal Loops, *21st International Conference on Environmental Systems*, San Francisco, California, July 15-18, 1991, SAE Technical Paper Series;

[8]. Birur G.C., Bhandari P. et al., Mechanically Pumped Fluid Loop Technologies for Thermal Control of Future Mars Rovers, *36th International Conference on Environmental System (ICES)*, Norfolk, Virginia, July 17-20, 2006, SAE Technical Paper Series, 2006-01-2035;

[9]. Birur G.C., Bhandari P. et al., From Concept to Flight: An Active Fluid Loop Based Thermal Control System for Mars Science Laboratory Rover, *42nd International Conference on Environmental Systems*, 15-19 July 2012, San Diego, California, AIAA 2012-3514;

[10]. *Curiosity Rover Mission Overview*, https://mars.nasa.gov/msl/mission/overview/, accessed Jan. 2021;

[11]. *nanoSPACE AG*, https://www.linkedin.com/posts/nanospace-ag_nanospace-pumps-spaceindustry-activity-6735275926688415744-eTek/, accessed Jan. 2021;

[12]. ISO 21940-11:2016 – Mechanical vibration – Rotor balancing Part 11 – Procedures and tolerances for rotor with rigid behavior, International Standardization Organization;

[13]. Neumaier, R., (1997), Hermetic pumps – The latest Innovations and Industrial Applications of Sealles Pumps, 1st edition, Elsevier Science;

A STUDY ON REDUCING THE ADHERENT DROSS ON ADDITIVELY MANUFACTURED CLOSED IMPELLER

Ionut Sebastian VINTILA[1], Alexandra ADIACONITEI[1], Radu MIHALACHE[1], Alexandru PARASCHIV[1], Tiberius FRIGIOESCU[1], Florentin CONDURACHI[1], Daniel DATCU[1]

ABSTRACT: The interest for the benefits of Additive Manufacturing (AM) technology is highly increased in all domains, especially in the space industry where the mass and budget constrains are critical points in the development of a space mission. This paper presents the approach to overcome the challenges occured during the manufacturing process of a closed impeller made of Inconel alloy (IN625) by Selective Laser Melting (SLM) technology. The closed impeller shall be integrated into a centrifugal pump designed for Mechanically Pumped Fluid Loop systems (MPFL) to be featured on spacecraft. During the printing process, a major concern was to avoid the deposition of support material in the internal passageways of the impeller, as it would be very difficult to remove it. Therefore, a specific defect was identified on the self-supporting surface (without support structure) – adherent dross, with an impact over the shroud thickness. To minimise the adherent dross on the shroud, a new building orientation was tested, and solid support material was placed between the shroud and the disc for the support structure attachment. The laser power was also reduced. Measurements were performed on the closed impeller samples and it was demonstrated that the laser power is directly linked to the adherent dross

KEYWORDS: additive manufacturing, closed impeller, selective laser melting, centrifugal pump, adherent dross.

NOMENCLATURE
AM   Additive Manufacturing
CAD   Computer-Aided Design
SLM   Selective Laser Melting
MPFL   Mechanically Pumped Fluid Loop
W/O   Without

---

[1] Romanian Research and Development Institute for Gas Turbines COMOTI, Bucharest, Romania

1. INTRODUCTION

The space industry is looking for advanced manufacturing technologies to create a challenging category of qualified products for launchers and satellites systems [1,2]. Unlike other industries, these components are designed to withstand extreme space environment and launch loads. The Additive Manufacturing technology generates complex geometries which can be easily customized for each application. The advantages as mass savings, aspect which has a strong impact on reducing the manufacturing costs, tooling and speed of innovation make the AM a promising technology to maintain a competitive environment in space industry. To meet the demanding requirements for a qualified space product as low mass and high stiffness, the Selective Laser Melting (SLM) technology should ensure products with high performances or at least comparable with the ones achieved by conventional methods. The entire process, also known as laser powder-bed fusion, consists in creating a work piece in a metal powder bed. This technology uses a laser beam as the heat source to selectively melt the metallic powder particles of the layer according to the CAD model. The material is re-solidified after a cooling phase. This process is repeated until the final geometry of the component is achieved [3]. Transferring the SLM from research domain into industrial manufacturing is not a simple process, as demanding industry standards need to be fulfilled [4]. The SLM is not completely free form builder as the inherent process difficulties can distort many part geometries, and a major design issue is the lack of understanding of these difficulties and their impact on the final SLM product.

This paper intends to highlight the inherent defect of SLM, which can be minimised, but not avoided as the adherent dross occurs on overhanging structures. Until now, there are a few studies that reported the research on adherent dross generated on SLM components. Di Wang et al. [5] studied the adherent dross on typical geometrical elements (round and square holes vertical to the Z axis) and the authors have demonstrated that the defect is directly related to building orientation, scanning speed and laser power. Also, Koutiri et al. [6] presents the impact of the SLM process parameters on the quality of printed surface. In the current study, this topic was analysed on a specific component – a closed impeller that shall equip a centrifugal pump for mechanically pumped fluid loop systems designed for spacecraft thermal control system. The closed impeller is the main component which influences the pump performances. Having a low volume, complex design which formative or subtractive methods are unable to produce, the capabilities of additive manufacturing process appears to be the most appropriate to achieve the desired performances and other life-cycle objectives.

The adherent dross was identified on the shroud of the impeller and different technical solutions were applied to minimise this type of defect: building orientation was tested, solid support material was used and the process parameters were modified.

2. ADHERENT DROSS MINIMISATION

As the objective is to additively manufacture a closed impeller meeting the corresponding roughness and dimensional stability requirements so that it can equip a mechanically pumped fluid loop (MPFL) system, the model of the closed impeller was defined in accordance with the recommendations and constraints specific to the AM process (minimum wall thickness, channels, holes and machining allowance). The design of the closed impeller includes an offset on the external impeller surfaces which will be removed through mechanical post-processes. No offset material was added on the internal surface area of the closed impeller. The AM design of the closed impeller is presented in Fig. 1.
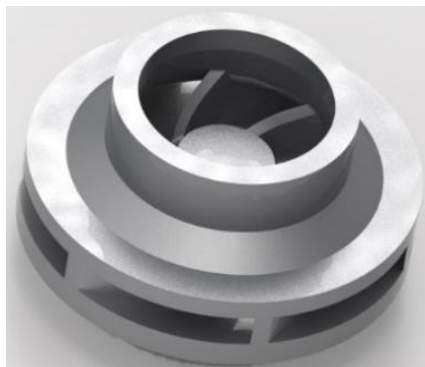
(a) Isometric view of the closed impeller model with offset material
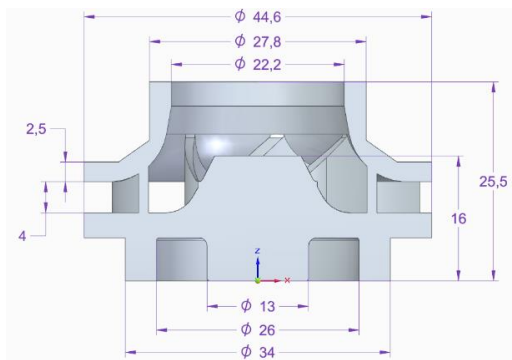
(b) Cross section view of the closed impeller model with offset material

Fig. 1 CAD model and dimensions of the closed impeller

The SLM process was carried out using a Lasertec 30SLM facility (supplier DMG MORI, Bielefeld, Germany) owned by Romanian Research and Development Institute for Gas Turbines COMOTI, with a building volume of 300 x 300 x 300 mm. During the fabrication of different AM closed impellers (the main process parameters are shown in Table 1, defined previously by Condruz et al. [7]), special attention has been addressed to the manufacturing process in order to avoid as much as possible the deposition of support material between the blades during the fabrication of the closed impeller. Therefore, different building orientation were used for the fabrication of the closed impellers, starting from orientation of Z axis (0° - parallel to the building plate) to B+32° and B+45°, previously studied in [8]. The terminology for building orientations is in line with standard terminology for additive manufacturing [9].

Table 1. SLM printing parameters

No.	Parameter	Value	Unit
1	Laser power	250	W
2	Scanning speed	750	mm/s
3	Layer thickness	40	µm
4	IN625 powder granulometry	15-45	µm

In paper [8], the authors presented the manufacturing process of closed impellers using SLM technology and during the evaluation process, a specific area characterized by a different colour with an aspect of an overheated material was identified on the shroud, as highlighted in Fig. 2. The defect also known as adherent dross was identified for the building orientation of B+32° and B+45°.
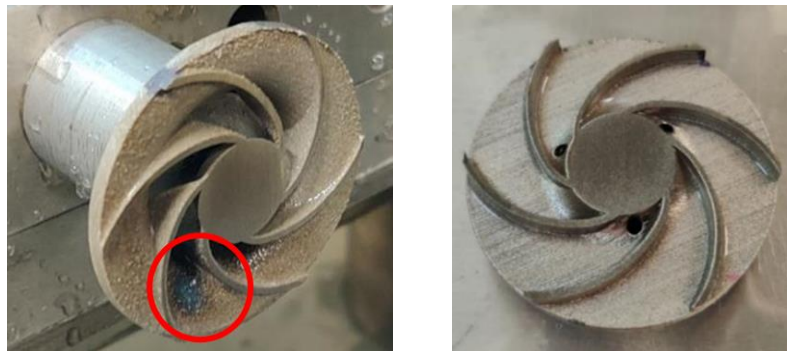

Fig. 2 Adherent dross observed only on the shroud of the closed impeller

To eliminate or minimise as much as possible the adherent dross, it is important to identify the parameters that cause the overheating of the area on the shroud. To observe if the phenomena appears for a specific orientation, flat specimens were printed at different building orientations, as presented in Fig. 3. The purpose of the plate specimens was to investigate the self-supporting surfaces and if the dross could be mitigated. Printing parameters are presented in Table 2. Flat specimens were considered in determining for which building orientation the overheated area appears, as it is less time-consuming than building different closed impellers for the same analysis.
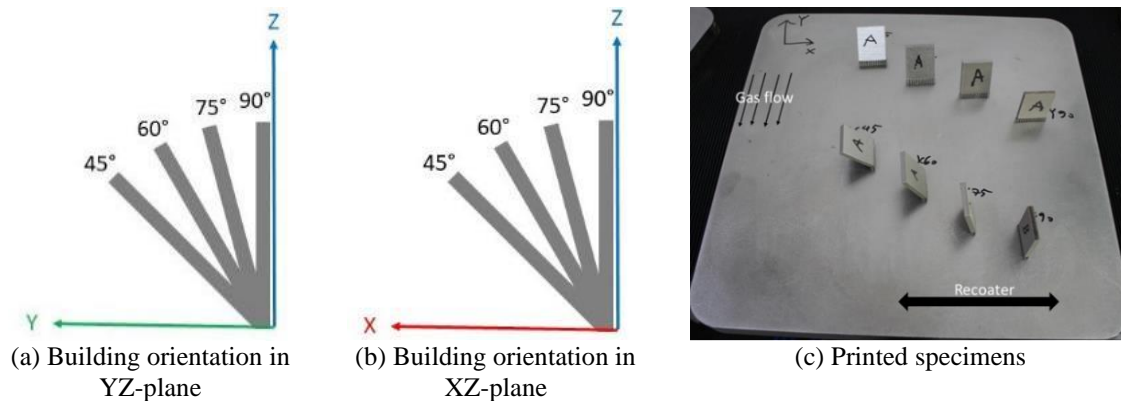

(a) Building orientation in YZ-plane   (b) Building orientation in XZ-plane   (c) Printed specimens

Fig. 3 Flat specimens on the building plate, on YZ and XZ planes

Table 2. Specimens printing parameters

No.	Parameter	Value	Unit
1	Dimensions of the specimens	25 x 30 x 4	mm^3
2	Laser power	250	W
3	Scanning speed	900	mm/s
4	Layer thickness	40	µm

It was observed that the overheated area appears on the lower side of the self-supporting surfaces, for angles between 45° (most pronounced) and 60° (less pronounced). Taking this into consideration, a possible method for minimizing the adherent dross for the closed impellers, it is to increase the building orientations to B+60°, to reduce the laser power and to add a solid support material between the blades. It is to be mentioned that the support material is not attached to the blades, a gap of 1 mm is left between the support material and the blade to avoid possible rupture or deformation of the blades during machining. Before adding solid material between the shroud and the disc, it is necessary, due to the very small dimensions of the closed impeller, to verify if the material can be eliminated. Thus, a milling simulation (Siemens NX CAM) is presented in Fig. 4, concluding that a solid support material can be added between shroud and the disc of 4 mm depth.
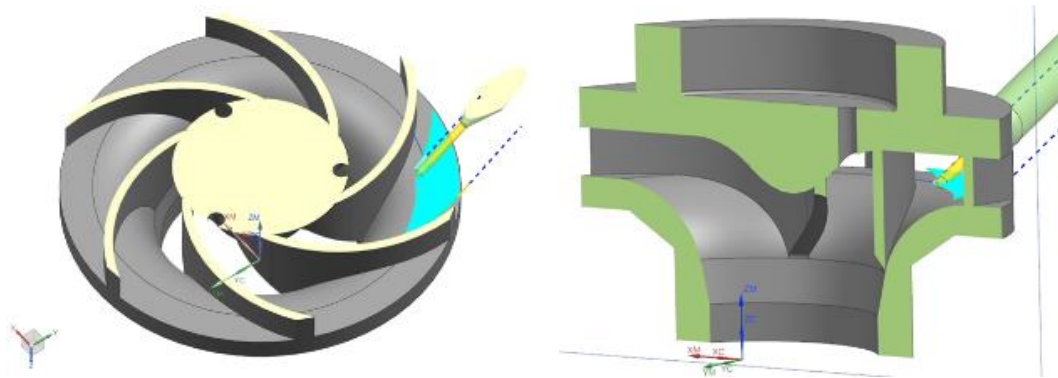

Fig. 4 Milling simulation of the support material (marked with light blue)

Considering the previously defined solution, the CAD model of the AM closed impeller was modified accordingly and it is presented in Fig. 5, along with the corresponding printed part. It was observed that the overheated area is significantly reduced when the changing of process parameters are combined with the B+60° XY-plane orientation and the solid support material between the shroud and the disc. For this printing iterations, as discussed above, the laser power was reduced to 200 W, while maintaining the same scanning speed and layer thickness as in the previous iterations.

Another iteration was considered, by further reducing the support material from 4 mm to 0.8 mm in order to be easily machined, as the overall offset material for AM was 1 mm. The process parameters were not modified. It was observed that the dross was reduced further and also the support structure could be easily machined during the post-processing activities.
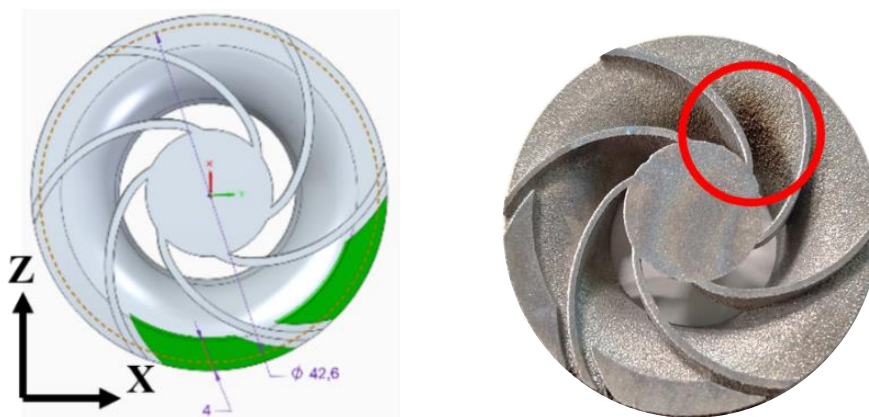
(a) CAD model and printed part for support material of 4 mm
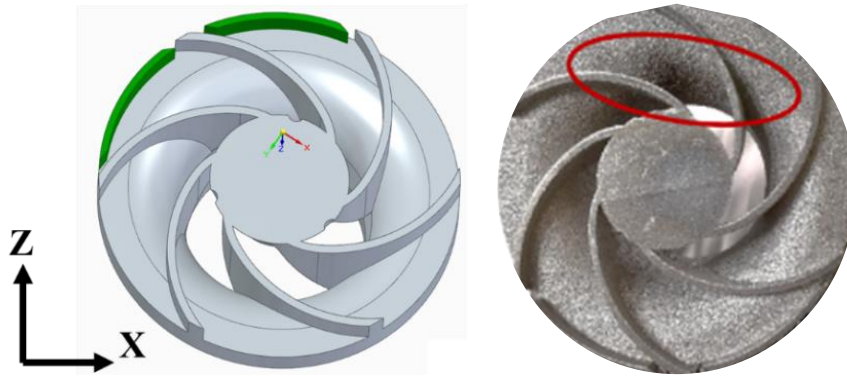
(b) CAD model and printed part for support material of 0.8 mm
Fig. 5 Closed impeller printed at B+60° with corresponding support material

In order to have a better understanding of the adherent dross and how it affects the part, two different areas from the same shroud were cut and analysed, as presented in Fig. 6. The dross and its effect on the shroud thickness were investigated based on measurements performed on optical images captured on both areas. Distance between successive measurements is 500 µm.
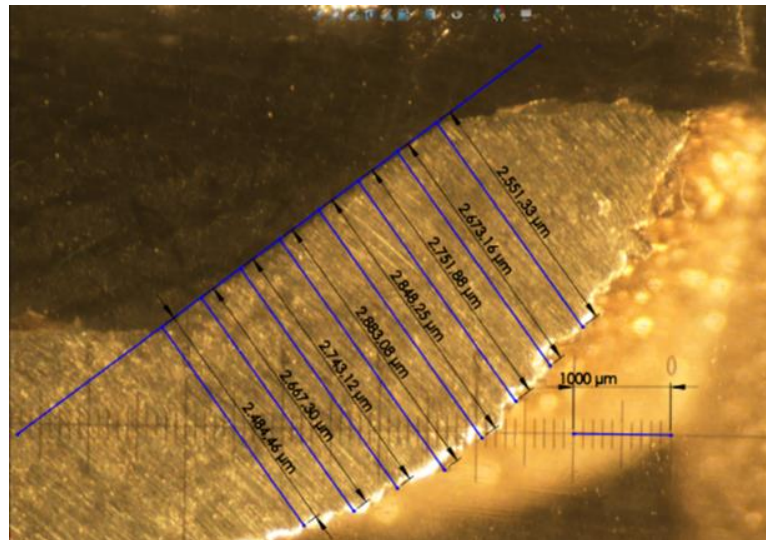
(a) Area 1 - without dross
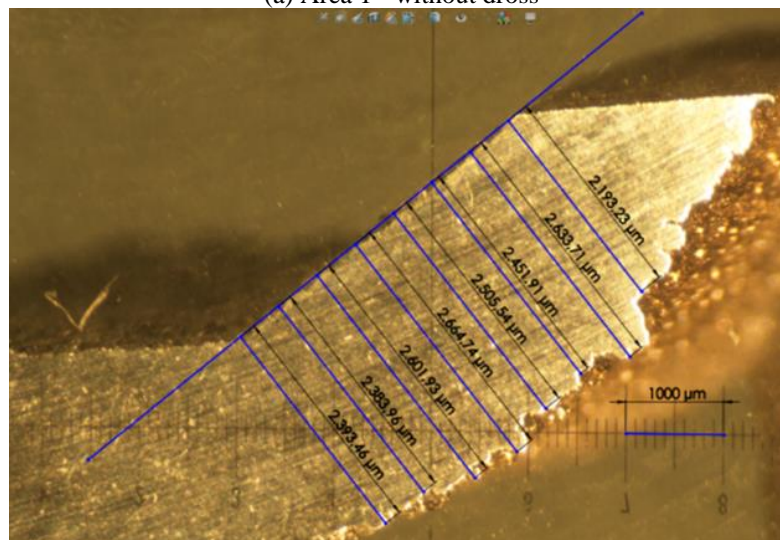
(b) Area 2 - with dross
Fig. 6 Sectioned area of the first specimen

The results of the adherent dross analysis are presented in Table 3 and also in Fig. 7. The maximum identified deviation between the area with dross and the one without dross was found to be 0.358 mm.

It is noticeable that there are relative high differences between the thicknesses of the two areas and the CAD model. The thickness of the overheated area (with adherent dross) is generally reduced compared to the one that was not affected by the dross and its associated area from the CAD model.

On the other hand, the thickness of the area without any traces of dross is higher than the thickness of associated area from the CAD model. These differences are mainly caused by the balling effect generated by the reduced laser power and printing accuracy. The balling effect is more pronounced in the area with dross and induces a higher surface roughness which may introduce additional errors. Furthermore, the measuring errors could be generated by the section plane which cannot be perfectly radial.

Table 3. Thickness of the dross area

Thickness area 1 (w/o dross) [μm]	Thickness area 2 (with dross) [μm]	Difference between area 1 and area 2 / CAD model [μm]	CAD Model [μm]
2551	2193	358	2240
2673	2634	39	2400
2751	2452	299	2530
2848	2505	343	2630
2883	2665	218	2690
2743	2602	141	2710
2667	2384	283	2590
2484	2393	91	2480
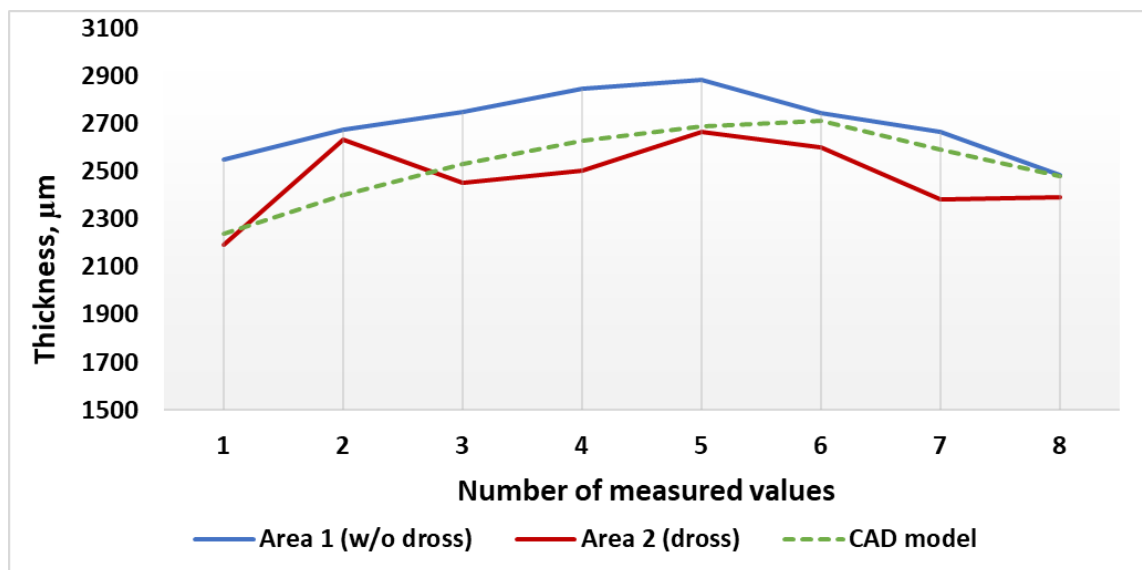
Fig. 7 Thickness differences between areas with and without dross

A second trial was made, maintaining the same thickness of support material and building orientation of B+60°, but reducing the laser power to 170 W and the scanning speed to 650 mm/s. The printed closed impeller was halved by electrical discharge machining (EDM) and the same analysis was performed. Fig. 8 presents the printed part (halved shroud) and the corresponding two areas cut from the shroud.
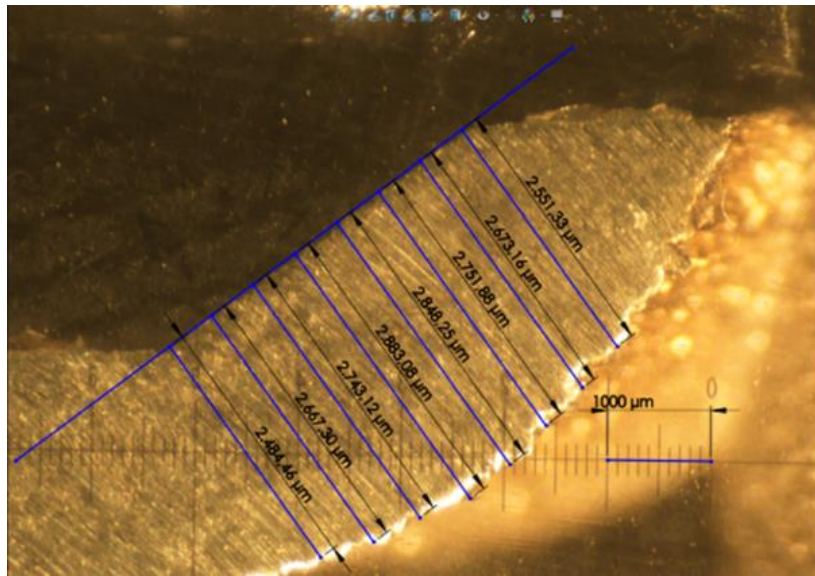
(a) Area 1 - without adherent dross
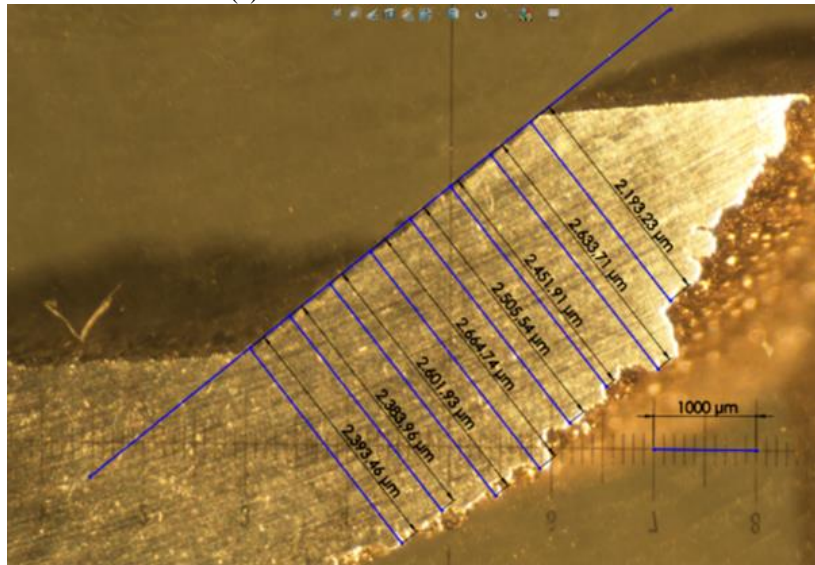
(b) Area 2 - with adherent dross
Fig. 8 Sectioned area of the second specimen

Table 4 presents the reference values for the CAD model, the thickness of the area without dross and the measurements for the thickness of overheated area. Distance between measurements was kept the same, at 500 µm.

Table 4. Thickness of the dross area

Thickness area 1 (w/o dross) [µm]	Thickness area 2 (with dross) [µm]	Difference between area 1 and area 2 / CAD model [µm]	CAD Model [µm]
2435	2164	271	2240
1957	1743	214	2026
2150	1962	188	2235
2304	2178	126	2404
2444	2583	-139	2534
2472	2535	-63	2628
2550	2620	-70	2688
2580	2690	-110	2714

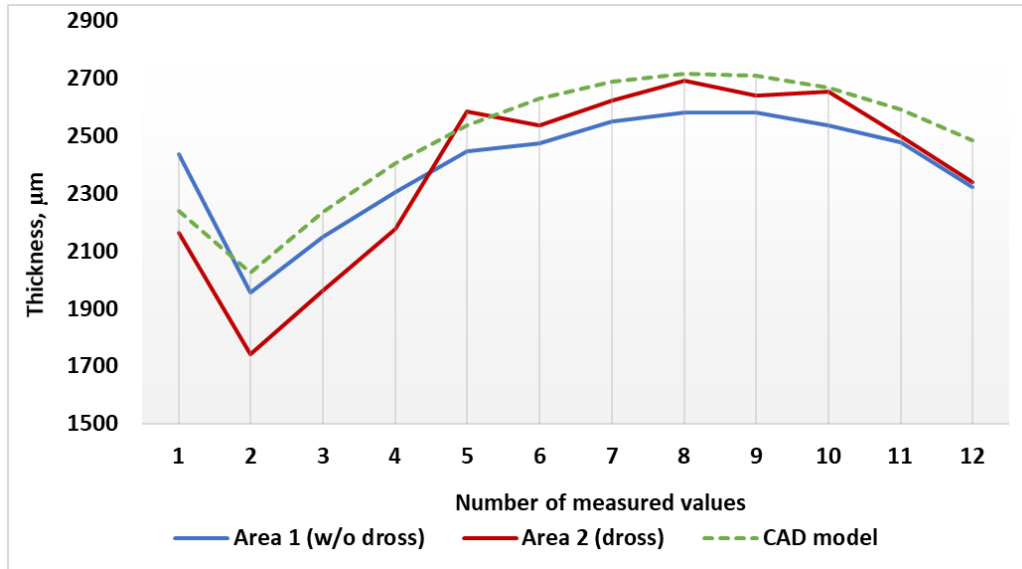**Fig. 9 Thickness differences between areas with and without dross**

Even though the laser power and scanning speed were significantly reduced, there are still differences between the thicknesses of the investigated areas. As presented in Fig. 8, the thickness of the overheated area is higher than the area that was not affected by the dross. Using a low laser power gave rise to the balling phenomena characterized by significantly coarsened balls possessing inherent structural weakness. A limited amount of liquid formation and a low undercooling degree of the melt due to a low laser input were responsible for its initiation.

The adherent dross minimization phase had a major impact on identifying the proper orientation and printing parameters. The proper orientation for the closed impeller is considered 60° in xy-plane with printing parameters presented in Table 5.

Table 5. Optimized process parameters

Orientation	Laser power [W]	Scanning speed [mm/s]	Layer thickness [µm]
60°	200	750	50

3. CONCLUSIONS

As the general objective of the study was to raise the knowledge towards increasing the technological readiness level of the additive manufacturing of complex metallic components for space applications, different challenges were encountered. One of these challenges is related to the appearance of an adherent dross area which could affect the mechanical properties of the closed impeller and possibly the overall performance of the MPFL system. Different dross mitigation solutions were proposed and performed, concluding that, by combining the addition of a thin, easily accessible and machinable support structure, finding of the building orientation and printing parameters, the adherent dross could be significantly reduced.

The appearance of adherent dross area can be also considered a technology shortcoming, based on the limitations of the SLM equipment. Also, the thermo-physical properties of IN 625 could be another aspect which generates the appearance of the adherent dross. In this regard, other materials such as Aluminium and Titanium alloy will be considered for the manufacturing of the closed impeller in the near future using the same technology.

ACKNOWLEDGEMENT

REFERENCES

 [1] S.S. Gill, Hemant Arora, Jidesh, Vire Sheth, *On the development of Antenna feed array for space applications by additive manufacturing technique,* Additive Manufacturing 17 (2017) 39-46, http://dx.doi.org/10.1016/j.addma.2017.06.010

[2] National Research Council. 2014. 3D Printing in Space. Washington, DC: The National Academies Press. https://doi.org/10.17226/18871.

[3] Nicolas Gardana, Alexandre Schneiderb, *Topological optimization of internal patterns and support in additive manufacturing,* Journal of Manufacturing Systems Volume 37, Part 1, October 2015, Pages 417-425, https://doi.org/10.1016/j.jmsy.2014.07.003

[4] Brandão, A.D.; Gerard, R.; Gumpinger, J.; Beretta, S.; Makaya, A.; Pambaguian, L. Ghidini, Challenges in Additive Manufacturing of Space Parts: Powder Feedstock Cross-Contamination and Its Impact on End Products T. *Materials* 2017, 10, 522 https://doi.org/10.3390/ma10050522

[5] Di Wang, Shibiao Wu, Yuchao Bai, Hui Lin, Yongqiang Yang, and Changhui Song, *Characteristics of typical geometrical features shaped by selective laser melting,* Journal of Laser Applications 29, 022007 (2017); https://doi/10.2351/1.4980164

[6] Koutiria, I.; Pessardb, E.; Peyrea, P.; Amloua, O.; de Terrisa, T. Influence of SLM process parameters on the surface finish, porosity rate and fatigue behavior of as-built Inconel 625 parts. *Journal os Materials Processing Technology* 2018, 255, 536–546, https://doi.org/10.1016/j.jmatprotec.2017.12.043

[7] Condruz, M.R. Matache, G. Paraschiv, A. Frigioescu, T.F. Badea, T., Microstructural and Tensile Properties Anisotropy of Selective Laser Melting Manufactured IN 625. *Materials* 2020, 13, 4829. https://doi.org/10.3390/ma13214829

[8] Adiaconitei, A., Vintila, I.S., Mihalache, R., Paraschiv, A., Frigioescu, T., Vladut, M., Pambaguian, L., A Study on Using the Additive Manufacturing Process for the Development of a Closed Pump Impeller for Mechanically Pumped Fluid Loop Systems, *Materials* 2021, 14, 967. https://doi.org/10.3390/ma14040967

[9] ISO/ASTM 52921:2013 Standard terminology for additive manufacturing — Coordinate systems and test methodologies, ISO/ASTM international 2013

Manufacturing of 3D printed lenses

Emilia PRISĂCARIU[1], Cosmin SUCIU[1], Razvan NICOARA[1], Marius ENACHE[1], Cristian DOBROMIRESCU[1]

ABSTRACT: This paper analyzes the possibility to locally 3D print lens blanks followed by mechanical post-processing in order to turn it into useful optical lenses. A comparison between two different methods is presented. The first method uses only one post-processing step by dipping the lens back into clear liquid resin, the same resin used for printing it. The second method applies polishing steps and precise layers of coating to try and reduce the material defects appearing in the first case. The printed lenses are afterwards tested and some of their characteristics are determined. The material used is conventional clear resin for SLA which means the equipment does not need to be adapted to a new type of material, granting the fact that the technology aspires to produce useful optics for engineering applications.

KEYWORDS: additive manufacturing, fining, coating, polishing, material treatment

NOMENCLATURE

UV- ultraviolet
IR- infrared
CNC - computer numerical control
EFL- effective focal length
S1, S2- surface1, surface 2
λ – wavelength
n- refractive index
A, B, C, D, E, F, G- variable numerals
a, b, c, d – variable numerals
℃ **-** degree Celsius
AC, PC, RN – geometrical segments
BN – propagating meridional ray
Z – curvature sag
r - radius of curvature
c - curvature
f'- focal length for a weak lens
Q - perpendicular distance from surface vertex
U - meridional ray slope angle
c_1 – first cap curvature
c_2 - second cap curvature
v_{c1} - first cap volume

I – angle of incidence
U - angle of refraction
I' - angle of incidence for the refracted ray
U' - angle of refraction for the refracted ray
SLA – stereolithography

1. INTRODUCTION

The concept of 3D printed lenses has been taken into consideration during recent years due to material science evolution. There are companies producing 3D printed optics, but their technology is based on inkjet printing, the technology being commercially oriented and the main product being produced by this technology represents prescription lenses. Fig.1 depicts Luximprint's new printing machine results, compared to the commerically available 3D printers. One advantage of the inkjet manufacturing technology is the ability to integrate smart-glasses technology into the lens during the printing process. Apart form the inkjet technology, there are many patents regarding 3D printing optics with a filament printer. Printing optics with a filament printer relies on the optical behavior of the inside-forming cylinders.
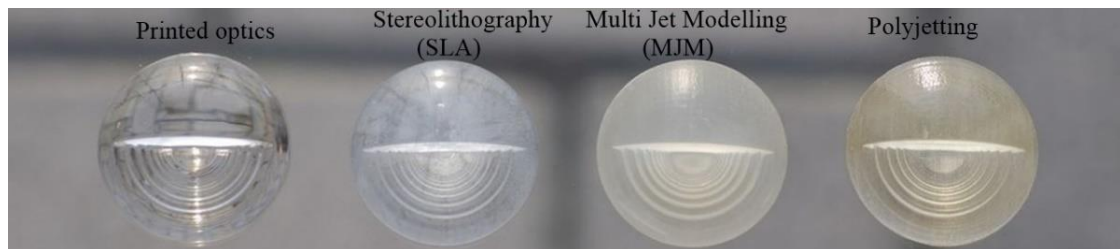

Fig. 1 Optically clear Luximprint resin to hardly transparent polyjetted filaments[1]

The manufacturing process applied in this study, contains 3 important steps: the optimization of the 3D model geometry, the post processing of the 3D lens blank, coating and other material treatments applied in order to better the optical quality or expand the lifespan of the lens.

The main advantage of developing a manufacturing methodology based on additive manufacturing is the possibility to customize and scale the 3D model's geometry, optimizing the interior layer deposition as well. The exterior of the lens can always be post-processed but the optical properties of the interior layers is an aspect that needs prior attention.

The conventional manufacturing process reaches its goal after completing 30 processing steps. Usually, the glass lenses are manufactured out of lens blanks. These lens blanks have a predefined face. This sets the future characteristics of the lens. For example, the pre-defined face can be either convex or concave. A mid-sized lens-manufacturing company has to stock approximately 10,000 lens blanks [2]. The conventional line uses a CNC machine in order to create the desired curve of the lens.

After the curvature is shaped and the lens blank has both sides defined, the surface processing step can take place on the conventional line. In order for the fining and polishing steps to take place, the lens must be placed on a polishing surface with the opposite curve of the lens. This special fining and polishing tool is called lap. There are special laps for each type of lens. [2]

An alternative to CNC machining is using the free form line which heats the lens blanks to its melting point in order to obtain the desired curve. The free form line uses a special water jet cutting machine. This also requires a thick lens blank in order to allow curve shaping by grinding the back. A cutting-edge polishing technology is presented in Fig.2.

The lens blank exiting the free form line has a very good roughness, and therefore, the fining stage can be skipped. The lens blank moves towards the polishing step.[3]

The lenses are afterwards exposed to a series of treatments, such as: anti-reflective coating, anti-scratching, spin coating in order to deposit a thin UV film, applying blue blocking coating, etc.

Fig. 2 Schneider Polishing machines [2]

New polishing technology relies on the process and not on the form of the tool. Intelligent calculation routines that precisely compute lens specific tool paths and dwell time profiles.

Reflections take place on both sides of the lens, causing a light loss between 4%-6% of the incident light's value. Through anti-reflective coating, the light loss can be diminished to a 0.5%. This type of coating is achieved by applying one or multiple layers of dielectric material. High refractive index (between 1.8-1.9) prescription lenses, are not recommended without the anti-reflective coating [4][5]

2. DESCRIPTION OF THE 3D MANUFACTURING PROCESS

a. Optical aspects

In this article, the manufacturing process starts by firstly applying the basic geometry modeling.

The lens final form must respect the next principle: all the rays in all wavelengths originating at a given object should be made to pass accurately through the image of that point. [6]

The lens parameters available for the lens designer are called "degrees of freedom". These degrees can be, based on the application: the radii of curvature, the refractive indexes and the dispersive powers of the glass used to separate lens elements (in the case of lenses systems), the "stop" position or aperture-diaphragm and the lens mount.

For the final element to have the desired characteristics, the focal length and magnification factor must aways be maintained by varying other parameters.

Establishing the thickness is the next step into obtaining a final geometry for the 3D model. Center thickness is easily to fix in the case of negative power lenses and it should represent about 6% to 10% out of the lens'diameter. For the positive lens, the center thickness has to take into account the following: for a lens diameter of 1-3 inches, 1mm should be left for grinding the lens, 1 mm will be removed while edging the lens and 1 mm per radius is used for placing the lens into the support mount. There are, of course many types of mounts and one has to make sure that the mount does not vignette any rays.

Weak lens surfaces are easier to produce, the radius of curvature allows one to fine and polish multiple lenses simultaneously.

The next step is to set up tolerances. The table below is usually used in doing so. Table 1 contains tolerances for plastic materials used by G.S. Plastics Optics. [6]

Table 1. Optics Manufacturing Tolerances for Plastic Optics by G.S. Plastics Optics [6]

Attributes	Tolerances (rotationally symmetric elements less than 75mm in diameter)
Radius of Curvature	±0.5%
EFL	±1.0%
Diameter	±0.020mm
Center Thickness	±0.020mm
Wedge	<0.01mm
S1 to S2 Displacement (across the molding parting line)	<0.020mm
Surface Figure Error	≤ 2 fringes per inch (2 fringes= 1λ)
Surface Irregulrity	≤1 inch per fringe (2 fringes= 1λ)

Surface Dig Specification	40-20
Surface Roughness Specification	<50Å
Diameter to Thickness Ratio	<4:1
Center Thickness to Edge Thickness Ratio	<3:1
Part to Part Repetability (one cavity)	<0.50%

The refractive index is a ratio between the speed of light through a specific medium and its speed through air. The refractive index of a lens varies with each wavelength. For an optical material, the refractive index given in the lens' specifications is true for the specified wavelength, but in the case of using the lens in other conditions, a relation between n and λ must be established.

The three equations needed for this relationship to be defined, are:

$$n = A + \frac{B}{\lambda^2} + \frac{C}{\lambda^4} \tag{1}$$

$$n = A + \frac{B}{\lambda} + C/\lambda^{7/2} \tag{2}$$

$$n^2 = A + \frac{B}{\lambda^2-C^2} + \frac{D}{\lambda^2+E^2} + \frac{F}{\lambda^2-G^2} + \cdots \tag{3}$$

In the visible spectrum, the Cauchy relation (1) can define the graph as a straight line because the third term is really small.

In order to solve the system for A, B,C, Conrady (2) and Helmholtz (3) must be used as well. From (3) , $n \rightarrow \infty$ when λ= C, E, G, etc., these values of λ become asymptotes that mark the center of the absorption lines.

If the binomia theorem is applied to (3), the following is obtained:

$$n^2 = a\lambda^2 + b + \frac{c}{\lambda^2} + d/\lambda^4 + \ldots \tag{4}$$

In (4), a contains the infrared indices ($\lambda \gg$), and c,d, the ultraviolet indices ($\lambda \ll$).
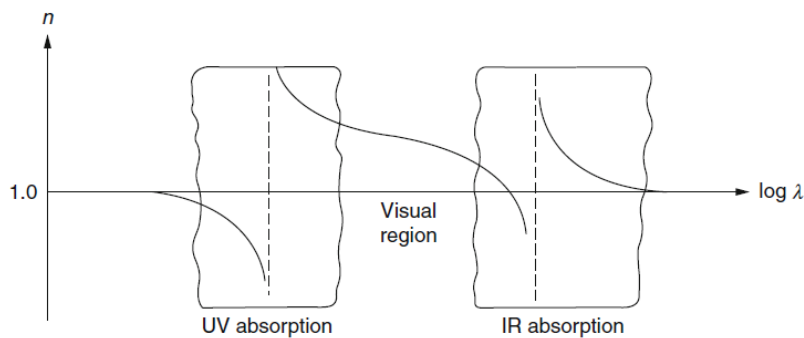

Fig. 3 Relation between the refractive index of a glass and the log of the wavelength [5]

Also, changes in refractive index appear while using the lens in a temperature varying medium. For glass, the refractive index varies very little (about 0.000001 per °C). In the case of plastic materials, this variation becomes significant. In the range of 0-40°C, the refractive index has a 0.0056 variation which significantly alters the focus.

In order to trace a ray through the lens, some basic considerations have to be taken into account. There are 3 types of rays: meridional (the meridional plane is defined as the plane passing thrugh an extraaxial point and the lens axis), paraxial (these are very close to the optical axis and considered to be negligible) and skew rays (these never intersect the lens' axis).
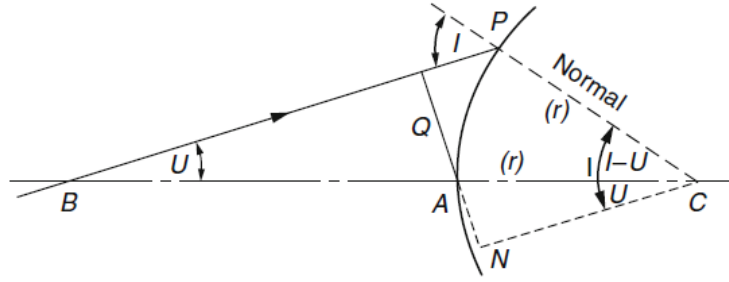
Fig. 4 Refraction of a meridional ray at a sphere[5]

Because the lens to be manufactured is a bi-convex lens, the trigonometrical lens tracing at a spherical surface be performed.

From Fig.4 one can calculate I between the ray and the normal. r=AC=PC, and can be observed that CN is parallel to the ray. This helps writing the following:

$$Q = rsinI - rsinU \tag{5}$$

Where Q is the perpendicular distance from surface vertex and U is the meridional ray slope angle.

$$sinI = \left(\frac{Q}{r}\right) + sinU \tag{6}$$

$$sinI' = \frac{n}{n'} + sinI \tag{7}$$

$$PCA = I - U = I' - U' \tag{8}$$

$$U' = U + I' + I \tag{9}$$

$$Q = r(sinI' - sinU') \tag{10}$$

From (6)-(9), U' and Q for the refracted ray can be extracted. Apart from performing ray tracing, one can calculate the volume of a lens. This is important in the process of 3D printing in order to optimize the used material. The volume calculation of a bi-convex lens can be achieved by splitting the lens into 3 elements: 2 spheric caps and a cylinder. [7]

Calculating the caps is done by applying the formula:

$$v_{c1} = \frac{1}{3}\pi Z^2(3r - Z) \tag{11}$$

Where Z represents the surface sag and r is the radius of curvature. The volume of the cap has the same sign as the optical form. For a positive (convex) cap, the volume is positive, and for a negative (concave) cap, the volume is negative. The cylinder volume is calculated traditionally. All the above calculations can be applied to the 3D geometry model.

Another important factor to be considered is the calculation of the magnification.This is done by applying the Lagrange theorem. The magnification calculation is done in 2 different ways: transversial and longitudinal. The lens bending has to be implemented in lens calculation, the main advantage of bending is that through it one can change a singular variable of the lens, while keeping the rest. The focal length of a thin lens is described by Eq. (12) [8].

$$\frac{1}{f'} = (n - 1)(c_1 - c_2) = (n - 1)c \tag{12}$$

(12) describes the way one can vary the c value and solve for c_2. [5]

b. **Pre-printing test**

a)   b)   c)
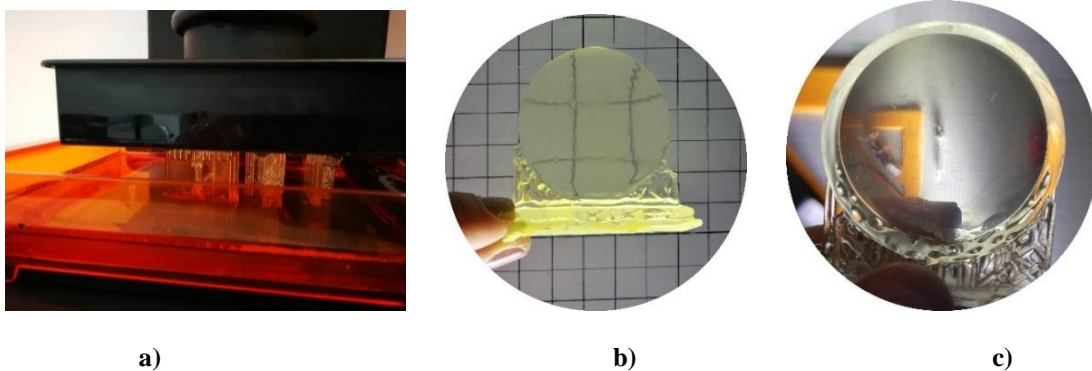**Fig. 5 a) Formlabs3 3D Printer, b) unpolished bi-convex lens, c) unpolished bi-concave lens**

The 3D printed lenses in Fig.5 are dipped into melted clear resin after printing in order to create a coating layer that improves the optical quality of the lens, but this procedure results into an uneven layer and does not solve for the other issues of the model, like: the fact that the deposition layers can be observed, the added supports influence the lens' edge, and overall, the lenses provide a distorted image of the object, as observed in Fig. 6.

These lenses were printed as a test to see if the material is clear enough so that after polishing it could become more transparent and useful in the optics printing process. The newly developed manufacturing technology and its stages are detailed in the next chapter.
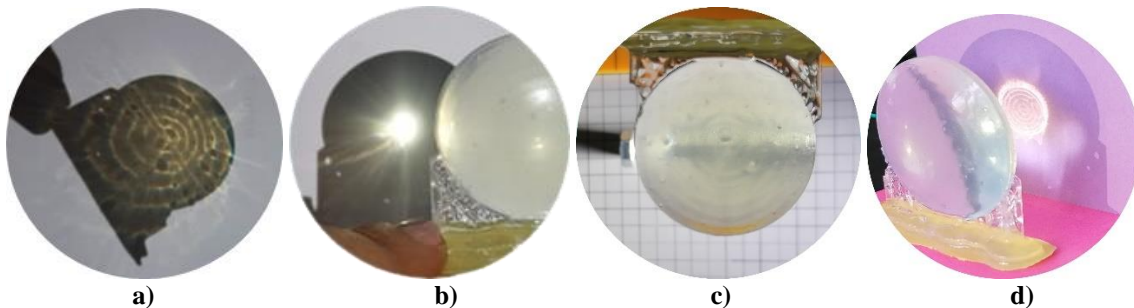

a)   b)   c)   d)
Fig. 6 Optical issues:a) air bubbles inside the material, b) optical coma, c)deposition layers, d) bad imagining of the point-like light source (images taken at INCDT COMOTI)

3. GEOMETRY MODELLING AND SURFACE POLISHING

The desired 3D printed lens is a bi-convex lens.The bi-convex lens surface is obtained by intersecting 2 spheres with the same diameter. The intersection is done taking into account the desired surface to be obtained.

For a bi-convex lens with c =0.04, c_2= -0.02 and c_1=0.02, one can determin the focal length, if the refractive index is known (n=1.58 is the refractive index of the clear resin used for printing). This results in a focal length equal to $f' = 43,20mm$.

The thickness of the internal cylinder is 2mm. Because of the flatter surface, the lens is considered to be a weak lens.

The focal length can also be derived from the thin lens equation, but this requires a very precise measurement of the distance from the lens to the formed image of the object and is therefore less accurate.

Other considerations: the surface will lose 1 mm in the polishing process. The lens' volume is determined by the same software used to 3D model the lens, CATIA V5. One can also perform an optimization of the process, by controlling the parametric layers (as in Fig.7) or perform a slope analysis (see Fig. 8). The optimization program used is Creo Elements/Direct Modeling Express 8.0, and the optimization images as courtesy of INAS S.A.
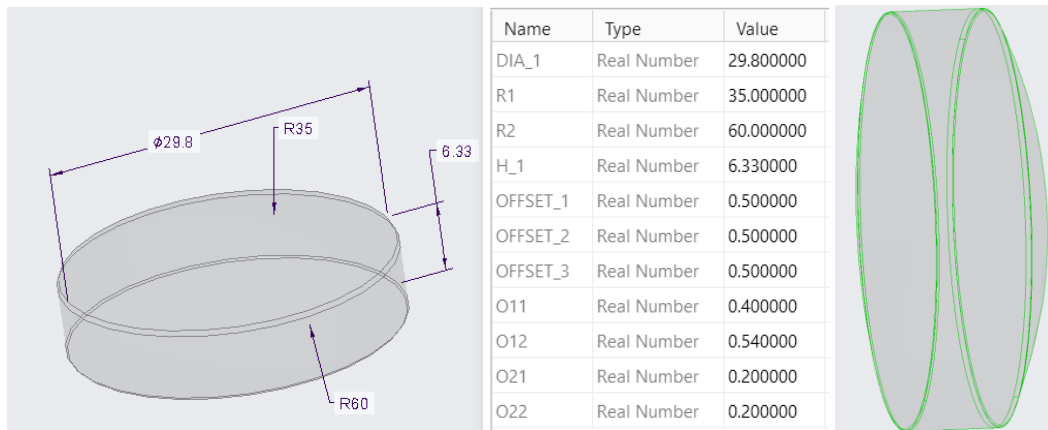
Name	Type	Value
DIA_1	Real Number	29.800000
R1	Real Number	35.000000
R2	Real Number	60.000000
H_1	Real Number	6.330000
OFFSET_1	Real Number	0.500000
OFFSET_2	Real Number	0.500000
OFFSET_3	Real Number	0.500000
O11	Real Number	0.400000
O12	Real Number	0.540000
O21	Real Number	0.200000
O22	Real Number	0.200000

Fig. 7 Example of parametric layers being added to the 3D model

The polishing lap must have the same curvature as the lens, in order for the original surface to be kept. The polishing material is fixed on the lap by a thin film of glue. The lens has to be polished one surface at a time, by using a clamp ring or other type of clamp.

The surface polishing steps to be applied are: fining (using sandpaper with a higher roughness, in this case 800), polishing (using polishing paste and felt), and finally spraying transparent-mat varnish in order to take the reflections off.

The fining process leaves the lens in a very little transparent shape. Approximately 1mm has been removed from its surface.

The polishing betters the lens and turns it slightly more transparent. 3 passes over each surface have been applied.
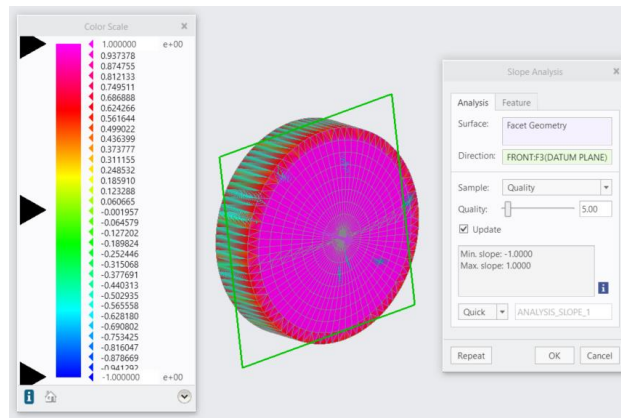

Fig. 8 Slope analysis for a convex lens

Table 2. Processes applied and results

	Process	Short description	Material used	Result
1.	Fining	Approximetly 3 passes over each surface	Sand paper roughness 800	

| 2. | Polishing | 3 passes over each surface | Polishing paste and felt | |
| 3. | Coating | Spraying uniformely 2 coats on each surface | Transparent mat varnish | |

4. CONCLUSIONS

The optical characteristics of the lens become better if the process is more precise and respects the 1µm deposition layer that needs to be deposited during the coating process. One important conclusion to be drawn is that if the coating material is applied in a thick layer, this can cause the lens to increase its opacity. The clear resin usually used for 3D printing cannot be used to print high precision optics, but if the application requires focusing the light at a given distance, one such lens can be used. Also, the issue of the refractive index modifying with temperature cannot be addressed here because the clear resin has a very low melting point. In the span of 0-100℃, the refractive index variation is negligible. The lens can be used in negative temperatures and is less sensitive to high temperature variations. Ray tracing is performed on the ideal 3D model, in order to solve for the meridional and paraxial rays that may apper, depending on the light source's scattering angle. This type of lens can be used in the pre-system to diminish the scattering angle, but on the downside, the light loss through it seams to be significant.

The polished version of the lens has good focusing capabilities. The dipped-in resin lens has a better sharpness of the resulted image, but the optical errors can be easily spotted. The criteria used to know which manufacturing technology is best, was visually analyzing the optical defects (like in Fig.6), and also establishing a comparison between the wanted focal length and the one that was obtained. For example, the focal length of the dipped in lens was shorter than the one previously set, and in the second case it was hard to determin it due to the unsharpness of the resulted image.

Testing was realized by causing a collimated light source to pass the lenses. To determin the focal length, the thin lens equation was used.

Table 3. Lens manufacturing technology comparison

	EFL (proposed) [mm]	EFL (obtained) [mm]	Image clarity (and focus)	Material defects
Dipped-in lens (a)	25	~23	Better than (a)	-
Polished lens (b)	25	>25	-	Better than (a)

Unfortunately, the observed differences between the effective focal lengths apply only to the two specific cases, not enough protoypes have been compared in order to draw general conclusions on the matter.

Future research will include an optimization of the polishing issue. Not polishing uniformly the curvature represents the main cause for poor image quality. Better equipments must be used in order to obtain a good surface and hence a better optical quality. Optical testing will be performed with a higher precision by optimizing the testing process.

REFERENCES

[1] John Larson, 2008, https://www.youtube.com/watch?v=yL_02Cxkmxk&t=218s

[2] http://www.3dprinting.lighting/category/3d-printed-optics/

[3] https://www.schneider-om.com/ophthalmics/polishing.html

[4] Matthew Parry-Hill, Robert T. Sutter and Michael W. Davidson - National High Magnetic Field Laboratory,The Florida State University - https://www.olympus-lifescience.com/en/microscope-resource/primer/java/lenses/lensvariations/

[5] Anthony Tangeman, 2014, *The Science Behind Anti-Reflective Coating,* *https://gosmarteyewear.com/blog/the-science-behind-anti-reflective-coating/*

[6] R. Kingslake, R. B. Johnson, *Lens Design Fundamentals*, VOL. I, SPIE Vol: PM195, Bellingham, Washington 98227-0010 USA

[7] E. Hecht, *Optics, Global Edition*, 5th Edition, Pearson Higher Education, California, USA

[8] M. Born, E. Wolf, 1999, Principles of Optics: Electromagnetic Theory of Propagation, Interference and Diffraction of Light, 7th Edition, Cambridge University Press, Cambridge, UK

INTEGRATED MECHANISM FOR SIMULTANEOUS ADJUSTMENT BETWEEN INLET GUIDE VANES AND DIFFUSER VANES

Teodor STĂNESCU[1], Gabriel-Petre BADEA[1], Dan CIOBOTARU[1], Daniel UȘERIU[1], George-Iulian BĂLAN[1]

ABSTRACT: The blowers are machines that transform the mechanical energy received from the electric motor into pressure energy. Regardless of the type of application in which the pneumatic machine is used, both the existence of a command and control system and the existence of a system for continuous regulation of the discharged gas flow are required. The regulation of the flow at the centrifugal blowers can be achieved by: the variation of the electric motor speed, the use of a "by pass", the parallel operation of several blowers, the modification of the suction flow section, the use of the inlet guide vane and the vane diffuser, etc. The flow control system that uses an inlet guide vane and a vane diffuser has the advantage of independent flow and pressure regulation. The article presents an integrated mechanism for operating the variable vane diffuser (VVD) blades depending on the position of the variable inlet guide vane (VIGV) blades.

NOMENCLATURE

$VIGV$	Variable Inlet Guide Vane
VVD	Variable Vane Diffuser
p	Pressure
Q	Volumetric flow
η	Yield (efficiency)
P	Power
CFD	Computational Fluid Dynamics

1. INTRODUCTION

Centrifugal blowers is a dynamic machine type, which achieves pressure energy using a centrifugal rotor [1]. In operation, in order to vary the flow, different methods can be used, among which we can list: the variation of the electric motor speed, the use of a "by pass", the parallel operation of several blowers, the modification of the suction flow section, the use of the inlet guide vane and the vane diffuser etc. By using the speed variation method, both the working pressure and the flow will change.

It is known that more than 50% of the total energy consumed by waste water treatment plants comes from compression units (blowers, compressors) [2]. One of the most efficient solutions (from the energetic point of view) for adjusting the flow when keeping the working pressure constant is found in the blowers that

---

[1]Romanian Research and Development Institute for Gas Turbines COMOTI, Bucharest, Romania

are equipped with VIGV and VVD system[3]. Fig. 1 shows a type of centrifugal blower that has in its assembly, VIGV blades, upstream rotor, respectively VVD blades, downstream rotor.

In the turbo-blower documentations presented by several manufacturers there are characteristic curves that describe the stable operating range of the machines, but there are no supply laws of efficient adjustments, or correlations between the angle of the VIGV blades according to the angle of the VVD blades, such that, the pressure is constant at flow variation [4]–[6].By performing experimental tests on a centrifugal compressor, Lee [7]pointed out that the same discharge pressures can be obtained for different combinations of angles between the IGV and VVD blades. Tests performed in [8] on a centrifugal compressor resulted in characteristic curves that express the dependence of the angle between the 2 stators in order to obtain a variation of the flow while maintaining a constant working pressure. In [3] is concluded that, for different pressure ratios, at a centrifugal compressor, the optimal efficiency curves differ.

Once the dependence curves of the angle of the VVD and IGV blades are known, obtained by experimental tests or numerical simulations (CFD), an integrated mechanism can be developed, which offers a strict dependence law of the blade angles with a single control point (a single actuator).

By using an integrated flow control mechanism, which modifies the VVD blades angle according to the position of the IGV blades angle, using a single actuator, linear or rotary, such that the cost of both production and energy, are reduced.
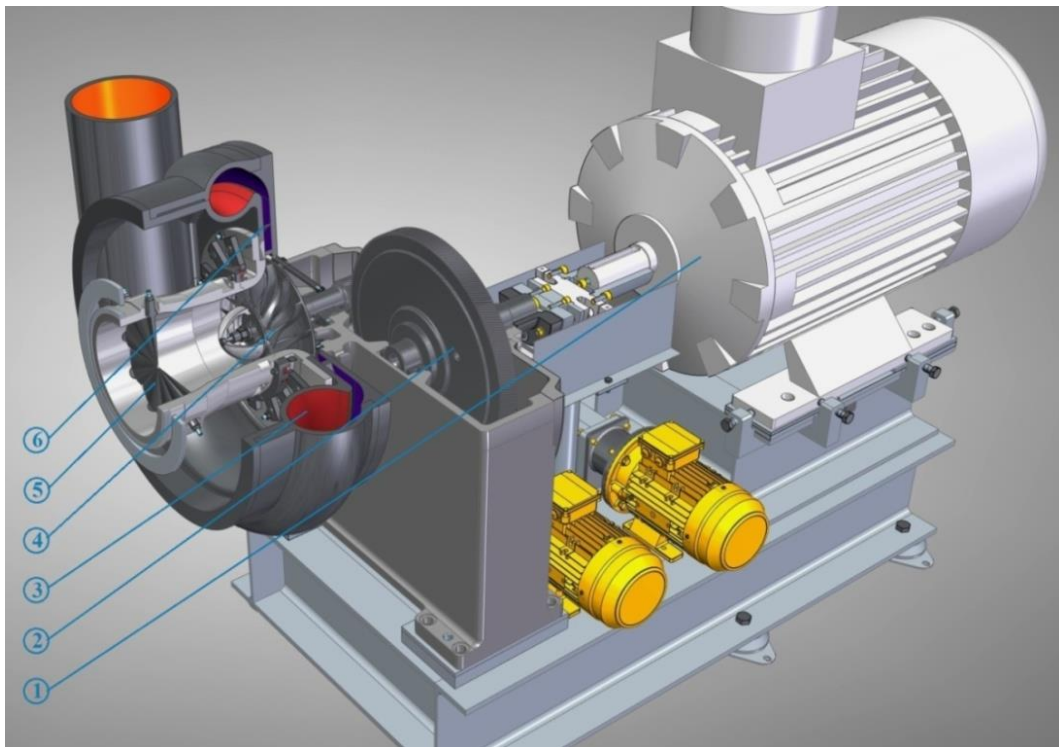
Fig. 1 Centrifugal blower with flow controlled by VIGV and VVD[9], where:
1 –Electric motor; 2 – Speed multiplier; 3 – Volute; 4 –Impeller; 5 – VIGV blades; 6 – VVD blades

2. Mechanism layout

The rotation of the VVD blades will be done according to the angle of the VIGV blades operated by a rotary / linear actuator. Fig. 2 lists the main components of the integrated VIGV-VVD drive system, and in Fig. 3 and 4 are shown the 2 views in which the variables of the mechanism (angles and lengths) are noted.
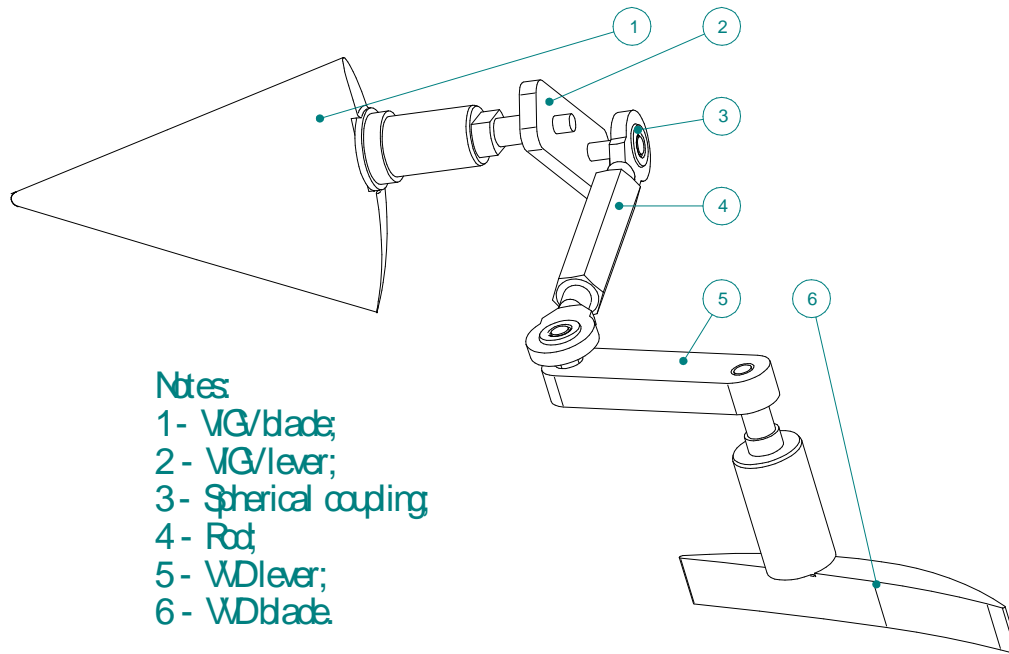
Fig. 2 The 3D model of the mechanism [9]

Notes:
1 - VIGV blade;
2 - VIGV lever;
3 - Spherical coupling;
4 - Rod;
5 - VVD lever;
6 - VVD blade.

The types of motions and components involved are:
- Revolution motion: VIGV blade (1), VIGV lever (2), VVD lever (5) and the VVD blade (6);
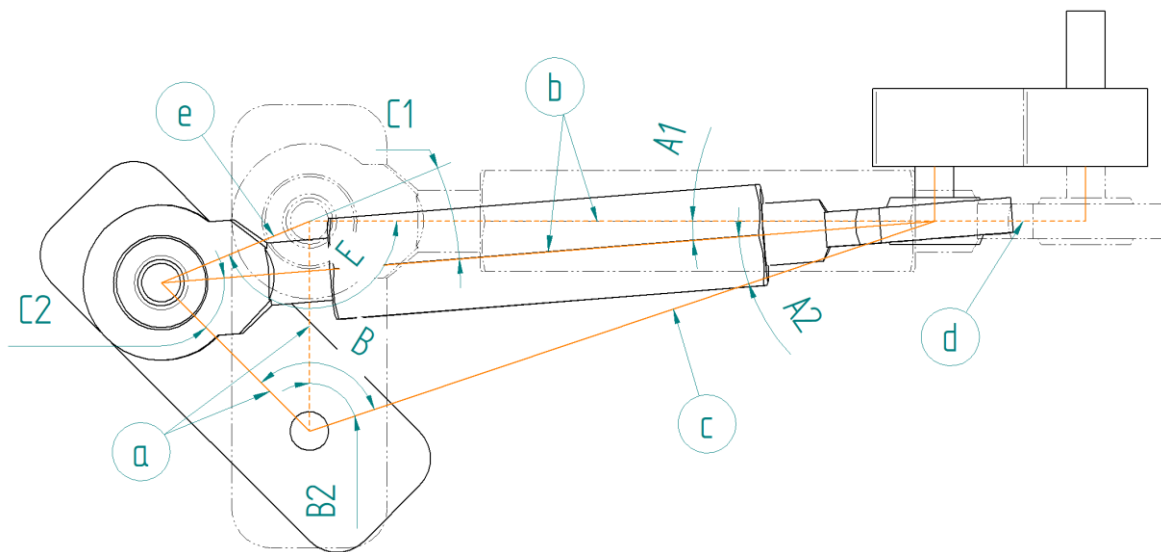- Plane-parallel motion: Spherical couplings (3) and the Rod (4).

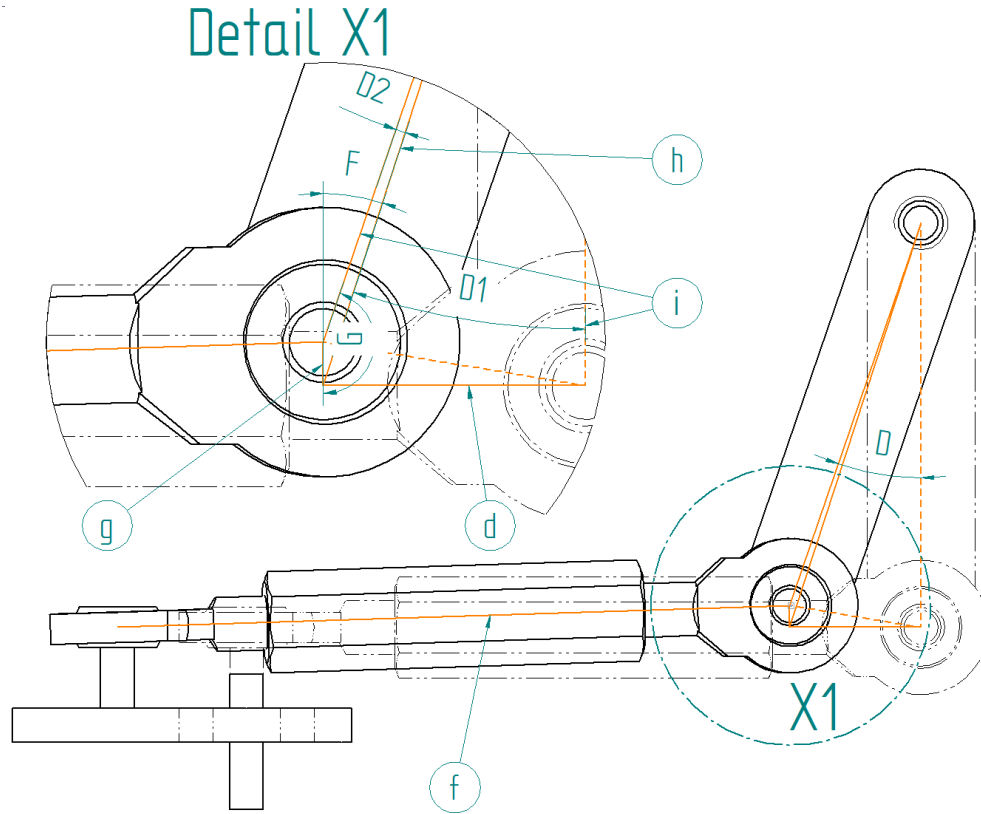**Fig.3 Front view of the mechanism [9]**

Fig.4 Sideview of the mechanism [9]

3. MATHEMATICAL CALCULATION OF MECHANISM[9]

Starting with the input data:
- a [mm] – the length of VIGV lever;
- b [mm] – the length of spherical coupling assembly;
- i [mm] – the length of VVD lever;

$$B_1 = \sphericalangle VIGV = \{0; 1; 2 \dots 88; 89; 90\} \, [deg] \tag{1}$$

The angle B_1 shown in Fig. 3 represents the angle at which the VIGV blades will tilt. This angle will vary, in our case, from 0 to 90 degrees. After the elements listed above are defined, we will proceed to determine the angles and sides of the triangles required to establish the variation of the angle of the VVD blades (kinematic movement of the mechanism) as follows:

$$C = \frac{180 - D3}{2} \, [deg] \tag{2}$$

$$F = \frac{180 - D3}{2} + 90 \, [deg] \tag{3}$$

$$e = \sqrt{2 \cdot a^2 \cdot (1 - \cos(B_1))} [mm] \tag{4}$$

$$A_1 = \text{asin}\left(\frac{e \cdot sin(F)}{b}\right) [deg] \tag{5}$$

$$C_2 = C - (180 - F - A_1)[deg] \tag{6}$$

$$c = \sqrt{a^2 + b^2 - 2 \cdot a \cdot b \cdot \cos(C_2)} \, [mm] \tag{7}$$

$$d = b - \sqrt{c^2 - a^2}[mm] \tag{8}$$

$$h = \sqrt{i^2 + d^2}[mm] \tag{9}$$

54

$$D_1 = \text{asin}\left(\frac{d \cdot sin(90)}{h}\right) [deg] \tag{10}$$

$$F = D_1 \tag{11}$$

$$G = 180 - \text{asin}\left(\frac{h \cdot sin(F)}{i}\right) [deg] \tag{12}$$

$$g = i \cdot cos(G) + h \cdot cos(F) [mm] \tag{13}$$

$$D_2 = 180 - G - F [deg] \tag{14}$$

$$D = D_1 + D_2 [deg] \tag{15}$$

$$\sphericalangle VVD = D [deg] \tag{16}$$

The calculation method presented above was made by neglecting the movement on the 3rd direction of the spherical couplings, the errors obtained by this hypothesis being $0 \ldots 1\%$.

4. RESULTS

A calculation model is presented in the following, a model in which it was desired that the VIGV blades angle fluctuates between $0\ldots90°$ and the VVD blades angle to have values between $0\ldots20°$.

Table 1 was made using the following values: $a = 34.4$ mm, $b = 100$ mm and $i = 118.7$ mm.

Table 1. The values calculated for the drive system shown in Fig. 2[9].

No.	Parameter	Unit	Value						
1	a	mm	34.4						
2	B_1	deg	0	5	10	...	350	355	360
3	b	mm	100						
4	i	mm	118.7						
5	C	deg	90	87.5	85	...	-85	-87.5	-90

No.	Parameter	Unit	Value						
6	F	deg	180	177.5	175	...	5	2.5	0
7	e	mm	0	3	6	...	6	3	0
8	A_1	deg	0	0.1	0.3	...	0.3	0.1	0
9	C_2	deg	90	85.1	80.3	...	-259.7	-264.9	-270
10	c	mm	105.75	102.92	100.12	...	111.42	108.59	105.75
11	d	mm	0	3	5.97	...	-5.97	-3	0
12	h	mm	118.7	118.74	118.85	...	118.85	118.74	118.7
13	D_1	deg	0	1.4	2.9	...	-2.9	-1.4	0
14	F	deg	0	1.4	2.9	...	-2.9	-1.4	0
15	G	deg	180	178.6	177.1	...	182.9	181.4	180
16	g	mm	0	0.04	0.15	...	0.15	0.04	0
17	D_2	deg	0	0	0	...	0	0	0
18	D	deg	0	1.4	2.9	...	-2.9	-1.4	0
19	$\sphericalangle IGV$	deg	0	5	10	...	350	355	360
20	$\sphericalangle VVD$	deg	0	1.4	2.9	...	-2.9	-1.4	0

Plotting the values of the VVD blades angle as a function of the values of the VIGV blades angle presented in Table 1, the dependence curve of the mechanism for the imposed values (lengths a, b and i) is obtained (see Fig. 5):
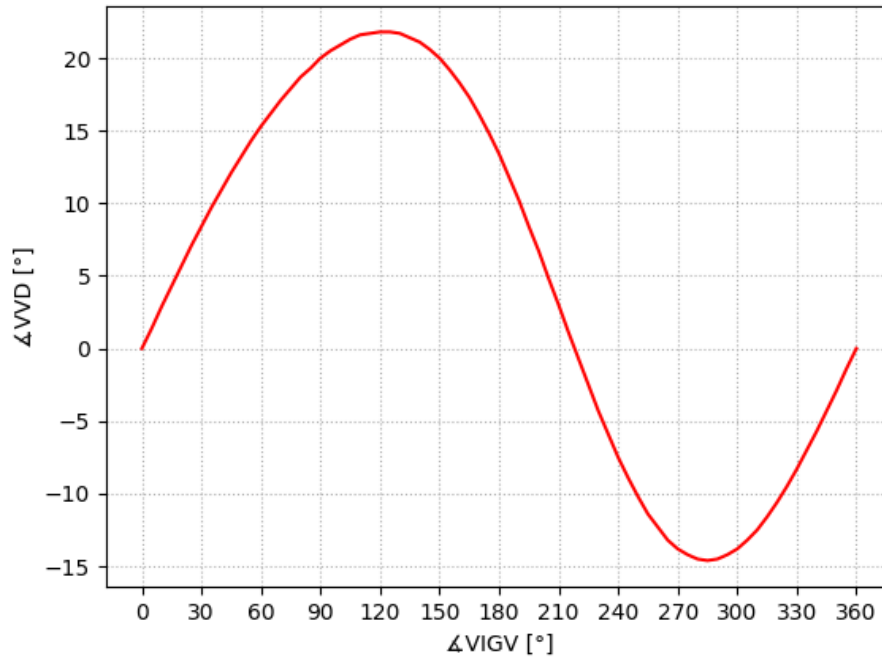

Fig. 5 Dependency of the VVD blades angle correlated with the VIGV blades angle

The sinusoidal shape of the curve is noticed. Depending on the initial position of the VIGV lever (angle B_1) several correlations can appear between the 2 angles ($\sphericalangle VVD = f(\sphericalangle VIGV)$). Because VIGV blades require a maximum angle of rotation of 90 degrees, Fig. 6 and 7 will be result. With the help of the centrifugal machine yield obtained from experiments or CFD numerical simulations depending on the positions of the VIGV and VVD blades, the shape of the VVD dependence curve can be established depending on the VIGV, this being adjusted from the initial position of the VIGV lever.
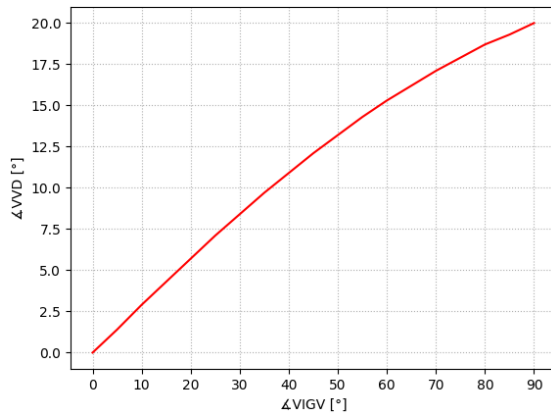

Fig.6 Dependency of the VVD blades angle correlated with the VIGV blades angle, with starting point of VIGV at 0°[9] ($\sphericalangle VIGV = 0 \dots 90°$)
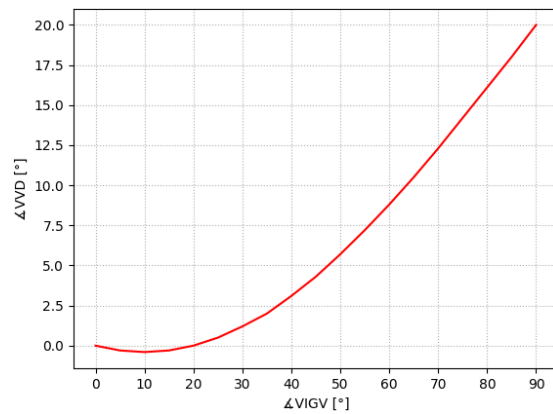

Fig. 7 Dependency of the VVD blades angle correlated with the VIGV blades angle, with starting point of VIGV at 270°[9] ($\sphericalangle VIGV = 0 \dots 90°$)

5. CONCLUSIONS

Following the research, it was concluded that by using an integrated flow control mechanism, which tilts the VVD blades according to the position of the VIGV blades, the costs of both production and energy are reduced by using a single control point (a single actuator).

The article presents an integrated flow regulation mechanism for centrifugal blowers, the constructive solution, as well as the kinematic calculation related to the mechanism.

A main disadvantage is that once the law of motion is established, by sizing the mechanism, it can be changed only by changing the initial angle of the first lever present in the mechanism.

Future research aims at the impact of the adjustment law of VVD blades according to VIGV blades on the reduction of energy consumption.

ACKNOWLEDGEMENT

REFERENCES

[1].   R. Braembussche, *Design and Analysis of Centrifugal Compressors*. 2019.

[2].   T. Xie and W. Chengwen, *Energy Consumption in Wastewater Treatment Plants in China*. 2012.

[3].   L. Zhou, G. Xi, and Y. H. Cai, "Experimental study on the influence of diffuser and inlet guide vane for the performance of centrifugal compressor," *Exp. Tech.*, vol. 32, pp. 26–33, Sep. 2007, doi: 10.1111/j.1747-1567.2007.00264.x.

[4].   "GL-Turbo." http://www.glturbo.com.cn/english/efficiency.asp.

[5].   "Driving Centrifugal Compressor Technology." https://www.atlascopco.com/content/dam/atlas-copco/compressor-technique/gas-and-process/documents/driving-centrifugal-compressor-technology-new.pdf.

[6].   "Turbo compressors and blowers brochure." https://www.howden.com/en-gb/lit/turbo-blowers-and-compressors.

[7].   L. Tetu, "Improving Centrifugal Compressor Performance By Optimizing Diffuser Surge Control (Variable Diffuser Geometry) and Flow Control (Inlet Guide Vane) Device Settings," Apr. 2021.

[8].   H. Simon, T. Wallmann, and T. Mönk, "Improvements in Performance Characteristics of Single-Stage and Multistage Centrifugal Compressors by Simultaneous Adjustments of Inlet Guide Vanes and Diffuser Vanes," *J. Turbomachinery-transactions Asme - J TURBOMACH-T ASME*, vol. 109, Jan. 1987, doi: 10.1115/1.3262068.

[9].   G. Badea, "Realizare model funcțional mașină paletată centrifugală cu control integrat VIGV-VVD. Teste preliminare. Corecții aduse modelului funcțional," *PN 19.05.02.01-5*, 2020.

The first flight of Romanian Turbo Jet.

On October 31st 1974, at IRAv Bacau aerodrome, an IAR 93A airplane powered by a turbo jet Viper Mk 632-41, made under Rolls Royce license, done the first fly.
Is Henri Coanda who arrange for Viper know-how transfer. The program IAR 93 has begun in May 20th 1971 as an agreement among Romania and Yugoslavia.
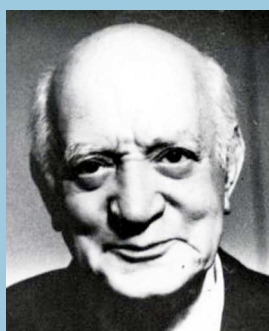
IT WAS THE FIRST JET FIGHTER
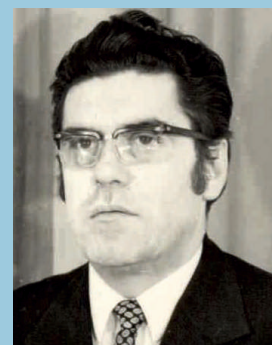designed & manufacturing by Romania after the WW2.

PASSION & COMPETENCE

Teodor Zamfirescu
Program Manager

Henri Coanda
Inventor of jet plane

Constantin Teodorescu
Entrepreneur for plane design

Eugen Pascariu
Entrepreneur for plane manufacturing

Gheorghe Stanica
Pilot

COMOTI

The only specialized company that integrates
such activities as

scientific research,
design,
manufacturing,
testing,
experimental activities,
technologic transfer and
innovation

in the field of aircraft and industrial gas turbines and
high speed bladed machinery.

220D Iuliu Maniu Ave., 061206 Bucharest, ROMANIA,
P.O. 76, P.O.B. 174
Phone: (+4)021/434.01.98, (+4)021/434.02.31, (+4)021/434.02.40
Fax: (+4)021/434.02.41, e-mail: contact@comoti.ro

www.comoti.ro